# Magnetic Resonance Imaging of the Brain:

# Enabling Advances in Efficient Non-Cartesian Sampling

by

Eric Aboussouan

A Dissertation Presented in Partial Fulfillment
of the Requirements for the Degree
Doctor of Philosophy

Approved November 2011 by the
Graduate Supervisory Committee:

David Frakes, Co-Chair
James Pipe, Co-Chair
Josef Debbins
Bruce Towe

ARIZONA STATE UNIVERSITY

December 2011

ABSTRACT

Magnetic Resonance Imaging (MRI) is limited in speed and resolution by the inherently low Signal to Noise Ratio (SNR) of the underlying signal. Advances in sampling efficiency are required to support future improvements in scan time and resolution. SNR efficiency is improved by sampling data for a larger proportion of total imaging time. This is challenging as these acquisitions are typically subject to artifacts such as blurring and distortions. The current work proposes a set of tools to help with the creation of different types of SNR efficient scans.

An SNR efficient pulse sequence providing diffusion imaging data with full brain coverage and minimal distortion is first introduced. The proposed method acquires single-shot, low resolution image slabs which are then combined to reconstruct the full volume. An iterative deblurring algorithm allowing the lengthening of spiral SPoiled GRadient echo (SPGR) acquisition windows in the presence of rapidly varying off-resonance fields is then presented. Finally, an efficient and practical way of collecting 3D reformatted data is proposed. This method constitutes a good tradeoff between 2D and 3D neuroimaging in terms of scan time and data presentation.

These schemes increased the SNR efficiency of currently existing methods and constitute key enablers for the development of SNR efficient MRI.

To my parents.

ACKNOWLEDGEMENTS

I have been fortunate to have had Dr. Jim Pipe as a mentor. His deep intuition and knowledge about MRI have shaped my understanding of the field during our many brainstorming sessions on the white-board.

My advisor Dr. David Frakes has been a great influence on me. I thank him for answering my numerous questions on signal/image processing, quantitative finance and entrepreneurship, often outside of the normal "business hours".

I want to thank Dr. Joe Debbins and Prof. Bruce Towe whose insights in the medical imaging industry (a.k.a. "the real world") I value greatly. Likewise, discussions with Dr. John Karis were helpful in providing me with a neuroradiologist's point of view.

I also thank all my colleagues at the Barrow Neurological Institute and Nick Zwart and Ken Johnson in particular for their assistance in my work.

Finally I am indebted to my parents for their constant support and encouragements.

TABLE OF CONTENTS

LIST OF TABLES

LIST OF FIGURES

Figure Page

Figure Page

Figure Page

# Chapter 1

# INTRODUCTION

Magnetic Resonance Imaging (MRI) is a versatile imaging tool for clinical diagnosis and scientific research but is limited in speed and resolution by the low Signal to Noise Ratio (SNR) of the underlying data. Reduction of scan times by factors of 2-6 without loss of image quality would be highly valuable as it would enable new applications and improve existing ones such as those that depend on temporal resolution or subject to motion artifacts (dynamic scanning, breath-held exams, etc.) Reducing total exam times would in turn increase patient acceptance and reduce health-care costs.

Parallel imaging (1), (2) and constrained reconstruction methods like compressed sensing(3) reduce the amount of data required to create unaliased images. These methods allow substantial speedups in scan time but face the physical constraint of the SNR loss that comes with less collected data. In order to regain this SNR without improvement to the hardware, more SNR efficient samplings methods are required. One way to do so is to acquire data during a higher proportion of scan time. These methods, however, often suffer from distortions that make them impractical for clinical use. The primary goal of this work is to develop enabling technologies that will allow the use of efficient sampling methods in the future. This work will focus primarily on neurological applications, and more specifically on diffusion imaging with full brain coverage, SPoiled GRadient echo (SPGR) spiral imaging and 3D orthogonal imaging methods.

Our strategy to improve Fast Spin Echo (FSE) diffusion scans with full brain coverage is to increase the fraction of the echo train duration used for sampling. This is done by switching from 2D to 3D multislab methods, thus reducing

the required TR. The scheme proposed in Chapter 4 improves on the SNR efficiency of FSE methods while limiting off-resonance distortions that hinder the use of common SNR efficient methods such as Echo Planar Imaging (EPI).

For SPGR scans, it can be shown that SNR efficiency is directly related to the proportion of scan time spent acquiring data. Very efficient SPGR scans already exist, such as spiral imaging with long acquisition windows. In practice, these scan suffer from severe blurring due to off-resonance and concomitant fields, especially when imaging the brain. The ability to obtain SNR efficient images of diagnostic quality is therefore directly related to the aptitude to deblur such images. In Chapter 6, an iterative method is proposed to substantially reduce the effects of blurring in the presence of fat and off-resonance fields of varying degrees of smoothness.

In some cases, 3D scan efficiency can be improved by recognizing that not all k-space is equally useful to acquire. This is the case when volumes are examined in reformatted, thick slices in orthogonal orientations. This observation constitutes the basis for Chapter 5 where a method is proposed to only acquire a subset of k-space while keeping SNR high and still allowing for parallel imaging calibration.

These methods have the potential to contribute to the future advance of SNR efficiency in common neurological MRI sequences.

# Chapter 2

# MAGNETIC RESONANCE IMAGING (MRI) PRIMER

This chapter will introduce Magnetic Resonance Imaging (MRI) to a general audience. After a brief historical perspective, the provenance of the MRI signal is explained and the concepts of spatial encoding, relaxation, contrast and echo formation are covered. A few common pulse sequences are finally described with focus on their applications. Emphasis will be made on visual explanations with high school level math only required for the section on relaxation.

## 2.1 What Is MRI?

MRI is a medical imaging technique that allows radiologists and other scientists to visualize the internal structure and function of the human body. Contrary to other medical imaging methods like x-rays and Computed Tomography (CT), MRI does not employ ionizing radiation, which greatly reduces its risk to long term patient health. Instead, MRI is based on the Nuclear Magnetic Resonance (NMR) phenomenon, a quantum mechanical property of atomic nuclei. MRI uses various magnetic fields to align the spin magnetization of key nuclei in the body. These nuclei then act like little antennas, emitting information-rich signals. Once sampled, these signals can be analyzed to reconstruct tissue images with a variety of contrasts along arbitrary cuts (Fig. 2.1) such as in Fig. 2.2.

## 2.2 Historical Perspective

As stated earlier, MRI is based on the NMR phenomenon first discovered by Isidor Isaac Rabi who showed that the spins of certain magnetic atomic nuclei can be forced to change their orientation using specific Radio Frequency (RF) pulses. While returning to their normal state, these nuclei release the absorbed energy by emitting their own radio waves.

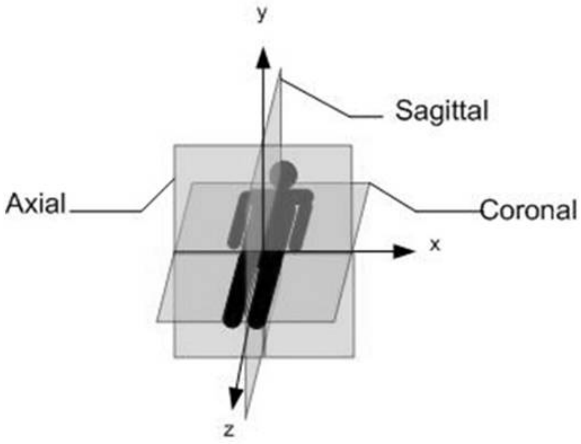


Figure 2.1: Definition of the standard radiological cuts

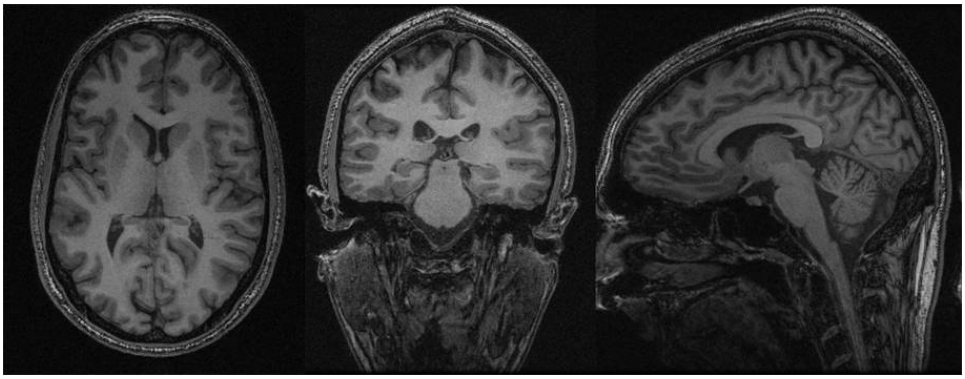

Figure 2.2: Brain MRI. Axial (left), coronal (middle) and sagittal (right) cuts of a healthy human brain

Rabi's work, which was rewarded by the 1944 Nobel Prize in Physics, was then refined by Felix Bloch and Edward Purcell who worked on the time evolution of the nuclear magnetization and showed how it could be used to identify the structure of molecules in solids and liquids. Their work deserved them the 1952 Nobel Prize in Physics.

Fueled by these developments, NMR quickly flourished. This was mainly due to the work of physicists such as Erwin Hahn and chemists such as Richard

Ernst who was awarded the 1991 Nobel Prize in chemistry for his development of NMR spectroscopy.

But NMR was still unable to retrieve spatial information from the studied samples. This changed in the early 1970s when Paul Lauterbur correctly recognized that adding linear gradients to his imaging magnetic field would provide spatial projections of the sample to be imaged. Inspired by Godfrey Hounsfield's Nobel winning CT projection reconstruction algorithm, he devised a way to reconstruct the first MRI image. This development was followed by Sir Peter Mansfield's invention of Echo Planar Imaging (EPI), a much more efficient way to acquire this information. Paul Lauterbur and Sir Peter Mansfield shared the 2003 Nobel Prize in Physiology or Medicine for their discovery of MRI.

Today, MRI research is a vast, multi-disciplinary field regrouping physicists, electrical engineers, clinicians, chemists, neuro-psychologists and biologists to name just a few.

## 2.3 Equation-Free Approach to Spatial Encoding

MRI spatial encoding concepts can seem arcane to newcomers but does not have to be. This section will attempt to explain some of the main concepts without the use of equations.

Imagine the simplified piano keyboard and equalizer pictured in Fig. 2.3[1]. This keyboard is linear in frequency (Fig. 2.4) and in amplitude (Fig. 2.5). Using this keyboard, we will proceed to show how a 1D shape can be encoded into a sound and then decoded.

When 2 or more keys are pressed together the signals are added (Fig. 2.6). The mathematical operation of sound formation is called a discrete Fourier Transform ($FT$). Inversely, the operation performed by bar equalizer to display

[1]The basic analogy was inspired in part by a talk by Alex Pines, chemistry professor at UC Berkeley, given at ASU on Feb 13, 2009.

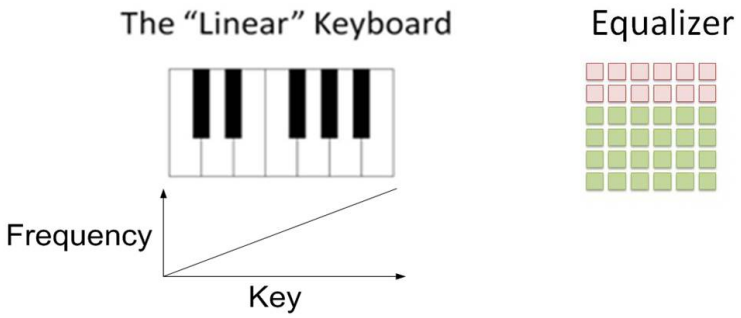


Figure 2.3: The linear keyboard (left) and the equalizer (right). The frequency of the sound varies linearly from left to right. The keyboard generates the sounds and the equalizer displays their frequency spectrum

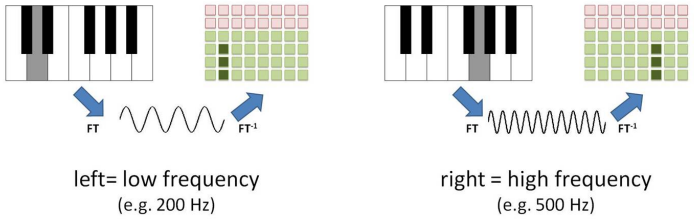


Figure 2.4: Linearity in frequencies. Ignoring the black keys and assuming that the tones made by the white keys vary linearly from the lowest frequency (left of the keyboard) to the highest (right of the keyboard) . This is what is called a spatial gradient of frequencies.

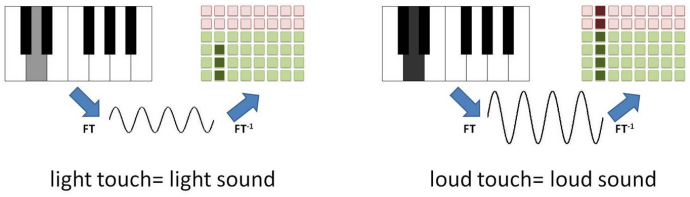


Figure 2.5: Linearity in amplitude. The harder a key is pressed, the louder the sound.

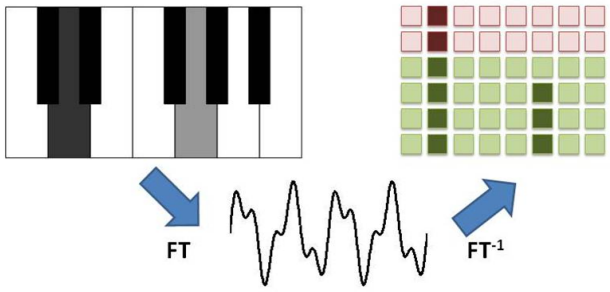


Figure 2.6: When 2 or more keys are pressed together their signals are added.

the frequency spectrum of the sound is called an inverse discrete Fourier Transform ($FT^{-1}$ ).

Like the linear keyboard, MRI spatial encoding uses a gradient of frequencies to encode the position of tissues. The signal is then acquired and inverse Fourier transformed to reconstruct the image. Although hard to visualize using keyboards, MRI spatial encoding can be generalized to 2D and 3D shapes.

A magnetic gradient is a spatial variation in the magnitude of the magnetic field but not in its direction. By analogy, a gradient in water current in a river does not change the direction but does changes the speed of the water (Fig. 2.7). Similarly, when a right/left magnetic gradient is applied to a sample, the rightmost spins will emit lower frequencies than the ones on the left. These signals will all add up and be detected simultaneously by the antennas of the MRI machine to be later reconstructed to form the image.

## 2.4 Relaxations and Contrasts

Imagine a toilet bowl[2] where the tank fills exponentially with time constant T1 and the water in the bowl drains with time constant T2. The tank represents a

[2]The basic analogy was inspired in part by a talk by Albert Mackovski at the Honolulu ISMRM Meeting in May 2009.

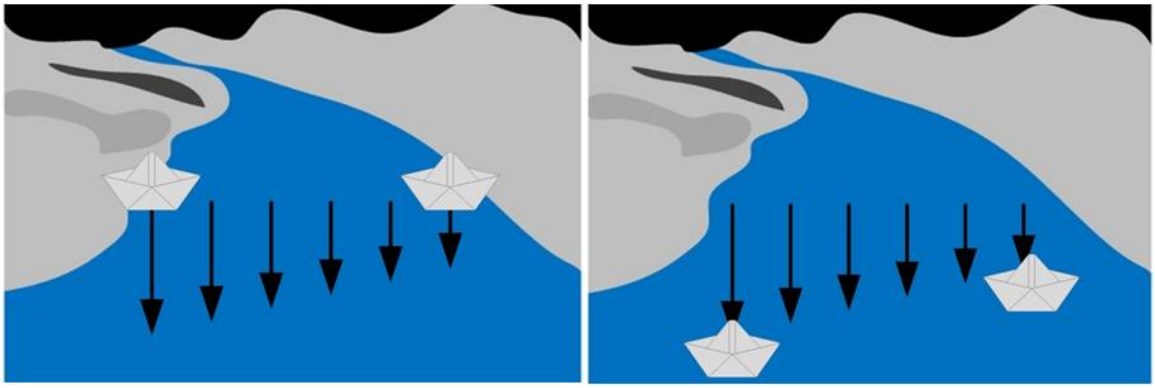

Figure 2.7: Gradient of water current. When two paper boats are placed in a right/left gradient of currents (left image) both boats move in the same downstream direction but with different speeds (right image).

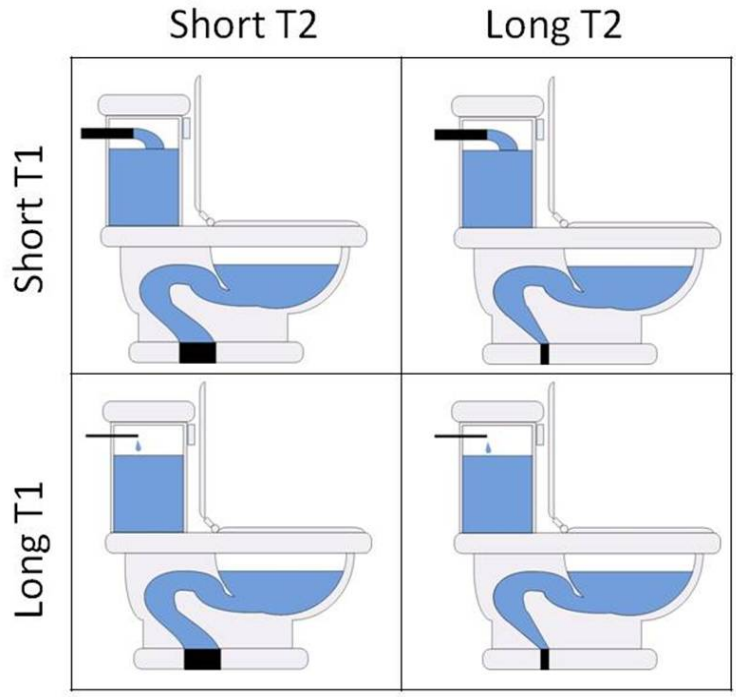


Figure 2.8: The toilet analogy. A toilet with "short T1" (top row) has a tank that fills up quickly. A toilet with "short T2" has a bowl that empties quickly (left column).

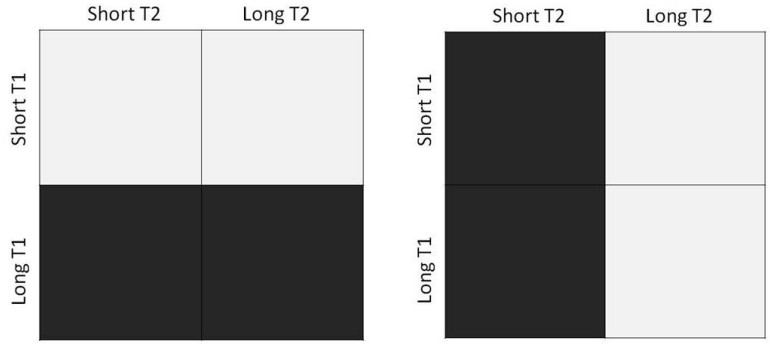


Figure 2.9: T1 and T2 contrasts. T1 weighted imaging (left image) and T2 weighted imaging (right image). Bright cells (high signal) indicate high water level in the bowl at time TE. Flushes are repeated every time TR. When TR is short, only the top row toilets will have substantial amount of water in their tanks, this is how T1 contrast is obtained. If TE is long, only the right row toilets will have water remaining in the bowl, this is how T2 contrast is obtained.

reservoir of signal which corresponds to the longitudinal magnetization $M_z(t)$. The water in the bowl corresponds to the rapidly decaying signal that is ready for acquisition in the transverse plane $M_{xy}(t)$.

$$M_z(t) = M_z(0)(1 - e^{-t/T_1}) \tag{2.1}$$

$$M_{xy}(t) = M_{xy}(0)e^{-t/T_2} \tag{2.2}$$

Some tissues have long T1, which means that their longitudinal magnetization (tank) recovers (fills up) slowly, and vice-versa. Some tissues have long T2 which means their transverse magnetization (bowl) decays (drains) slowly and vice-versa. Tissues can often be differentiated by their T1 and T2 relaxation times. In general, liquids tend to have long T1s and T2s whereas solids are the opposite. T1 relaxation curves for actual tissues are shown in Fig. 2.10 and T2 relaxation curves for the same tissues are shown in Fig. 2.11.

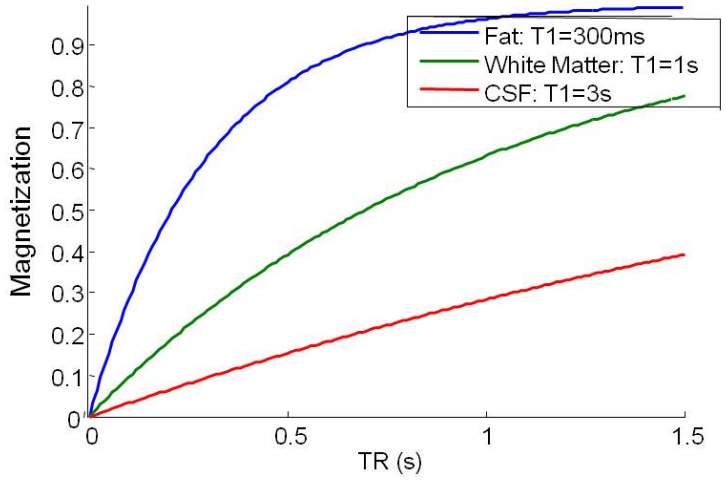


Figure 2.10: relaxation (recovery) curves for fat, white matter and CerebroSpinal Fluid(CSF)

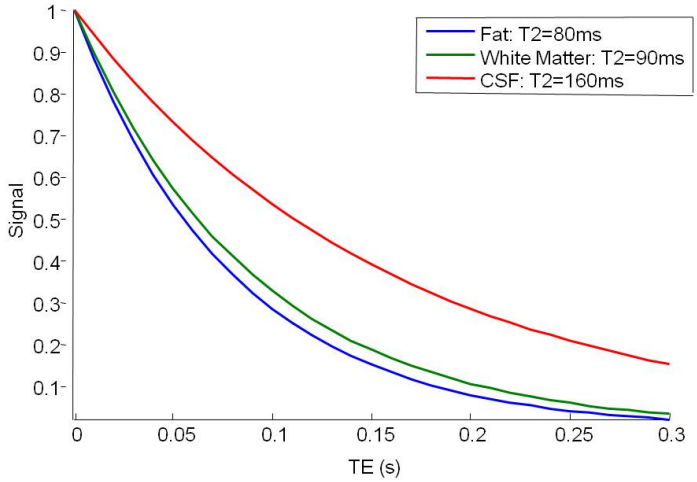


Figure 2.11: T2 relaxation (decay) curves for fat, white matter and CerebroSpinal Fluid(CSF)

Image contrast is defined as the ratio of the signals from two different tissues. The type and amount of contrast are mainly determined by sequence timing as measured with repetition time (TR), echo time (TE) and sometimes inversion time (TI). TR is the time between consecutive excitations of a given volume. The TR determines how much T1 recovery has time to take place on the longitudinal magnetization. TE is the time during which the transverse magnetization decays with a T2 time constant. In addition to TR and TE, some sequences include a inversion recovery preparation. These sequences invert longitudinal magnetization and let it recover for a duration TI after which the excitation occurs. Although most IR sequences are multi-slice sequences due to their long TR requirement, one exception is MPRAGE which is 3D.

Proton density is the most basic MRI contrast. When imaging with a short TE (<20ms) and long TR (>2sec) spin echo sequence, relaxation weighting can essentially be ignored. What is left is the density of water (and, therefore, water protons) in the imaged tissue. Since the popularization of Fluid Attenuated Inversion Recovery (FLAIR) sequences, proton density weighted imaging is rarely used in neuroimaging but it still has its niche in some Musculo-SKeletal (MSK) imaging applications.

T1 weighting is obtained by using a short TR (to increase T1 weighting) and short T2 (to decrease T2 weighting) or with the help of an inversion recovery preparation. Because of its short TR, T1 imaging is well suited for 3D imaging where rapid volumetric excitation result in shorter scan times. Nevertheless, T1 weighted 2D spin echo scans are still clinically used due to their ability to show blood flow. T1 scans offer high resolution and good gray-white matter contrast. Gadolinium contrast agents can also be injected to reduce T1 relaxation times of blood, tumors and other perfused tissues.

T2-weighting is obtained by using a long TR (to decrease T1 weighting) and short T2 (to increase T2 weighting). Because of its long TR, T2 imaging is well suited for multi-slice 2D imaging where interleaved slices are successively imaged and left to recover. T2 imaging is commonly used to image permanent brain injuries and lesions.

Besides anatomical imaging methods, MRI can also be used to observe physiological function. These MRI modalities include functional MRI (fMRI), angiography and perfusion imaging. Although other methods exist, fMRI usually employs susceptibility weighted imaging to detect the localized blood oxygenation levels in the brain. When a specific region of the brain performs a task, it receives increased blood flow with oxygenated blood (oxyhemoglobin). Oxygenated blood shows brighter than deoxygenated blood (deoxyhemoglobin) in susceptibility weighted imaging, thus allowing measurement of local brain activity. MR Angiography (MRA) employs a variety of methods to visualize the flow of blood. Some (but not all) MRA methods require injection of a gadolinium (Gd) based contrast agent. Perfusion measures (qualitatively or quantitatively) the amount of blood a given tissue receives. This is usually performed with the help of contrast agents.

Diffusion sensitized MRI pulse sequences are used to image the amount and preferential directions of diffusion in tissues. Clinically, Diffusion Weighted Imaging (DWI) is mainly used to detect and evaluate the extent of acute brain stroke. Although rarely done clinically, white matter integrity and fiber tracking information can also be obtained using diffusion imaging sequences. Diffusion Tensor Imaging (DTI) and Diffusion Spectrum Imaging (DSI) are among such promising schemes. Although all MRI pulse sequences are somewhat sensitive

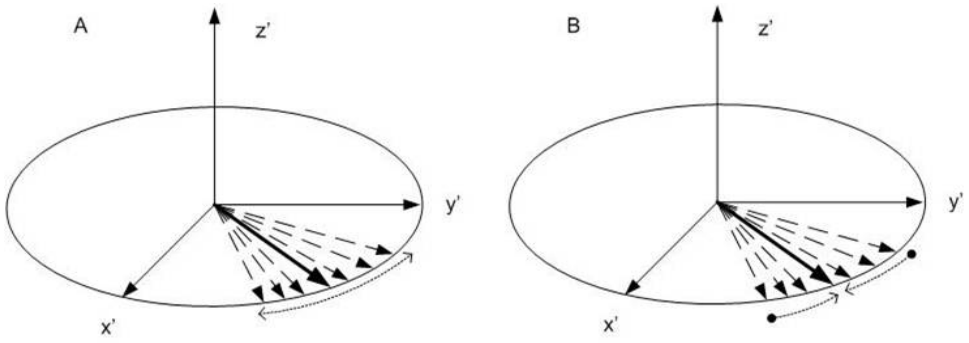


Figure 2.12: Dephasing and rephasing of the transverse magnetization. A) Dephasing, B) rephasing and echo creation

to diffusion, additional diffusion sensitizing gradients need to be added after excitation to make them diagnostically useful.

## 2.5 Pulse Sequences

### *Echo Formation*

MRI acquires images by subjecting the body to time varying magnetic fields. These magnetic field programs are called pulse sequences. There is a large variety of pulse sequences, each with their characteristics and properties. This section will give an overview of the main categories of sequences and the type of imaging contrast they can offer. The main pulse sequence classification is between gradient echo based and spin echo based sequences although many hybrids of these methods exist (spin-echo EPI, GRASE, ROTOR, etc.)

An echo happens when the transverse magnetization rephases (Fig. 2.12) thus emitting a signal of relatively high amplitude.

The gradient echo and the spin echo are the two basic echo generation methods (although others exist). The gradient echo happens when the magnetization dephased by an imaging gradient is subjected to the opposite gradient area. Although this can be done very fast, the gradient echo has the disadvan-

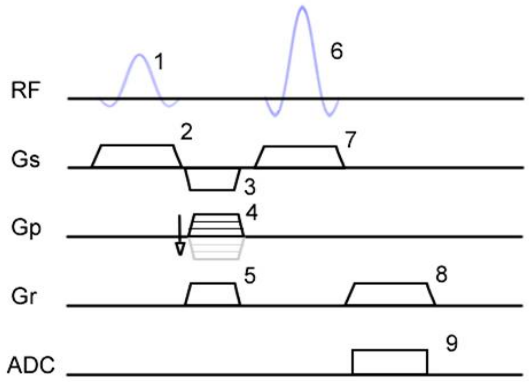


Figure 2.13: The basic spin echo sequence

tage of only refocusing the effects of the imaging gradient but not those of T2* and field inhomogeneities. The spin echo, on the other hand uses a RF pulse to invert all phase $\phi_{TE}(x, y, z)$ accumulated during a period TE at the beginning of which the magnetization was in phase (e.g. $\phi_0(x, y, z) = 0$). When subjected to the same gradients, the phase accumulated during the next period TE will still be $\phi_{TE}(x, y, z)$ but with a starting phase $\phi_{TE}(x, y, z)$ after the RF pulse. The total accumulated phase will be $\phi_{2TE}(x, y, z) = \phi_{TE}(x, y, z) - \phi_{TE}(x, y, z) = 0$ and we will get an echo.

*Introduction to Common Pulse sequences*

This section introduces some common pulse sequences with focus put on applications rather than physics and implementation. The reader should refer to subsequent chapters and references for a deeper understanding.

The basic Spin Echo (SE) is typically a T1 weighted sequence where a single line is acquired at each TR following a $90°$ excitation and $180°$ refocusing pulse. Although slow, SE presents very little artifacts.

After slice selective $90°$ excitation (Fig. 2.13.1) synchronized with the slice selection gradient (Fig. 2.13.2), a phase encoding gradient (Fig. 2.13.4)

is played. Rewinder gradients (Fig. 2.13.3 and Fig. 2.13.5) rephase the slice selection and prehase the frequency encoding. A $180^\circ$ (Figure 2.13.6) synchronized with a slice selection gradient (Fig. 2.13.7) refocusses the transverse magnetization. Finally, a readout gradient (Fig. 2.13.8) rephases the magnetization while Analogic/Digital Converters (ADC) digitize the signal received by the antennas (Fig. 2.13.9). The duration between excitation and the refocusing pulse is the same as the time between the refocusing pulse and the echo formation (TE).

Fast Spin Echo (FSE, aka Turbo Spin Echo, aka HASTE, aka RARE) uses a series of spin echoes to refocus the magnetization. As mentioned earlier, acquiring a line using a spin echo is much slower than using a gradient echo but has the advantage of refocusing not only the effects of the imaging gradient but also those of T2* and field inhomogeneities. Although not subject to T2* decay between echoes, the signal is still subject to T2 decay. Effective TE is defined as the TE of the central k-space line. Depending on the order in which acquired lines fill k-space, different types of image filtering will occur. A centric acquisition, for instance, acquires the center k-space line first which results in a decaying signal as we get away from the center of k-space. This has for consequence a low pass filtering of the image in the phase encoding direction. This filtering tends to limit the number of k-space lines that can be acquired after an excitation. For tissues with long T2, this filtering is less pronounced and acquisition of the full k-space after a single excitation (aka single shot) is even possible when imaging CSF. FSE is commonly used for T2 and diffusion imaging in the brain as well as abdominal and cardiac imaging in the body. Because of the long TR required, this has traditionally been a 2D multi-slice

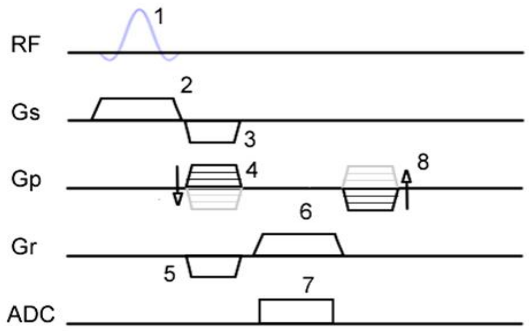


Figure 2.14: The basic gradient echo sequence

sequence. Recent advances in flip angle modulation and parallel imaging have, however, allowed 3D FSE sequences (CUBE) to see the light of day.

The basic gradient echo sequence (Fig. 2.14) prephases the magnetization in the readout direction (Fig. 2.14.5) following a small tip angle excitation and rephases it with an opposite readout gradient (Fig. 2.14.6) to generate the echo. Gradient echo sequences are classified in the ways they deal with residual transverse magnetization after readout. The magnetization can be RF spoiled (SPGR, FLASH), gradient spoiled (GRASS) or rebalanced (SSFP, FIESTA, True-FISP). Although for long TR imaging all gradient echo sequences are basically the same, for short TR, SPGR offers less signal at short TR but better T1 contrast than SSFP.

The SPoiled GRadient echo (SPGR, aka FLASH) is a gradient echo sequence that typically employs short TE, short TR and small flip angle. The transverse magnetization is RF spoiled to avoid residual signal from previous excitations. In its most basic form, this is a 3D T1 weighted sequence although T2 and T2* versions can be obtained. Common uses include high resolution T1 imaging of the brain, T2 detection of cerebral hemorrhage, angiographic/flow imaging, cardiac imaging (gated), dynamic susceptibility weighted (T2*) perfu-

sion imaging of the breast and fMRI.[MRI made easy]. With the exception of Musculo-SKeletal (MSK) imaging, body imaging uses mainly gradient echo sequences.

Echo Planar Imaging (EPI), originally introduced by Sir Peter Mansfield at the dawn of MRI, is an extremely fast method to fill k-space. Following excitation (and usually a refocusing pulse) several lines of k-space are acquired by a series of gradient echoes. Although very time efficient, EPI is very sensitive to image distortions and signal loss in the presence of field inhomogeneities. EPI is commonly used for fMRI and diffusion imaging.

FLAIR (Fluid attenuated Inversion Recovery uses a long inversion time TI ( 2s) to allow heavily T2-weighted FSE sequences by suppressing the cerebrospinal fluid (CSF) which would normally outshine other tissues. It can also be employed to improve T1 contrast. Because of the long TR required, FLAIR, like most IR sequences, is usually a 2D multi-slice scan where inversion and acquisition periods are interleaved. FLAIR is commonly used to look at edema (which is also liquid but has a different T1 than CSF), brain infarctions and Multiple Sclerosis (MS) lesions, among others.

Short TI Inversion Recovery (STIR) uses short inversion times ( 100ms) to suppress lipids and improve certain contrasts. Although a STIR preparation can be added to many different sequences (T1 or T2 weighted), it is more often employed with T2 Fast Spin Echo (FSE) to reduce acquisition time. STIR is commonly used to image the optic nerve and to show marrow edema in bone marrow and joint imaging.

Balanced SSFP (b-SSFP, aka FIESTA, aka TRUFI) is a gradient echo based sequence where the transverse magnetization is rephrased after each TR. This results in high signal compared to SPGR but also to a mixed (impure)

contrast and black band artifacts in the presence of field inhomogeneities. This sequence is commonly employed for rapid breath-hold imaging which has its uses in abdominal, cardiac and fetal imaging.

# Chapter 3

# IMPORTANT CONCEPTS IN MRI

## 3.1 The NMR Signal

Some atomic nuclei[1] possess a property called the 'nuclear spin'[2]. When a population of such nuclei is placed in a high enough magnetic field ($\vec{B}_0$), their spins tend to align with the field and create a macroscopic magnetic moment called magnetization. This magnetization acts like a little magnet which, at equilibrium, points in the direction of the field. By applying a time varying electromagnetic field ($\vec{B}_1$) to the sample it is possible to tip the magnetization away from its equilibrium position. The perturbed magnetization will then tend to return to its initial equilibrium state following a precession trajectory. Doing so, it emits radio-frequencies which are detectable by an antenna. This phenomenon is called nuclear magnetic resonance and the signal it produces is rich in valuable information that can be used to study the sample.

The most commonly used nucleus in MRI is the hydrogen nucleus which consists of a single proton. Roughly 60% of the human body is made of water molecules, which possess 2 hydrogen nuclei. Spins can find themselves in parallel or antiparallel configuration. The small surplus of parallel spins ( 6ppm at 3T) is responsible for the whole signal. The macroscopic vectorial sum of the magnetizations acts like a top precessing in space at the Larmor frequency ($\vec{f}$) given by:

$$\vec{f} = \hat{\gamma}\vec{B} \tag{3.1}$$

[1] All atom nuclei having an odd number of nucleons (protons and neutrons) and some having an even number of nucleons.

[2] This property can be deduced directly from the Schrödinger equation.

Where $\vec{B}$ is the local magnetic field and $\hat{\gamma}$ is the gyromagnetic ratio (42.576MHz/T in water). Off-resonance precession can thus be caused by two different factors: variations in and variations in . The first type is called chemical shift and is caused to small scale variation of the magnetic field around the nucleus due to electronic shielding[ref]. The most common chemical shift is seen in fat which precesses 440 Hz slower than water at 3T. The second effect is due to larger scale magnetic field variations usually due to magnetic susceptibility differences. Air/water boundaries and metallic objects are common causes of susceptibility differences.

The main field ($\vec{B}_0$ ) is aligned with $\hat{z}$, which is the axis of the MRI bore. In addition to this field, there are magnetic gradients that can be applied with various amplitudes in $x$, $y$ and $z$. The $(\hat{x}, \hat{y}, \hat{z})$ coordinate system is called the laboratory reference frame and is fixed with respect to the magnet (and the patient). To simplify calculations, we'll say that it is immobile in a rotating reference frame $(\hat{x}', \hat{y}', \hat{z})$, where $\hat{x}'$ and $\hat{y}'$ rotate around $\hat{z}$ at the Larmor frequency. The $\hat{z}$ axis is called longitudinal whereas the $\hat{x}, \hat{y}$ plane is called transverse.

## 3.2 The Bloch Equation

Without taking into account relaxation, the time evolution of the magnetization $\vec{M}$ subject to a magnetic field $\vec{B}$ is given by the Bloch equation:

$$d\vec{M}/dt = \gamma\vec{M} \times \vec{B} \tag{3.2}$$

With $\gamma = 2\pi\hat{\gamma}$ where $\hat{\gamma}$ is the previously defined gyromagnetic ratio. In matrix form, the Bloch equation is written:

$$\begin{bmatrix} dM_x/dt \\ dM_y/dt \\ dM_z/dt \end{bmatrix} = \gamma \begin{bmatrix} 0 & B_z & -B_y \\ -B_z & 0 & B_x \\ B_y & -B_x & 0 \end{bmatrix} \begin{bmatrix} M_x \\ M_y \\ M_z \end{bmatrix} \tag{3.3}$$

As noted earlier, gradients are used to linearly change the local magnitude of the z component of the magnetic field ($B_z$) in any spatial direction. Gradients are used, among other things, for spatial encoding.

While the gradients only affect $B_z$, the $B_1$ field (RF pulses) modifies $B_x$ and $B_y$:

$$B_z = B_0 + G_x x + G_y y + G_z z \tag{3.4}$$

$$B_1 = |B_1|(cos\theta + isin\theta) = B_x + iB_y \tag{3.5}$$

$$B_x = B_1 cos\theta \tag{3.6}$$

$$B_x = B_1 sin\theta \tag{3.7}$$

## 3.3 Radio Frequency (RF) Pulses

By applying a Radio Frequency (RF) pulse tuned to the Larmor frequency of a sample, it is possible to rotate its magnetization vector around an arbitrary axis in the transverse plane. One application of such rotation is to excite magnetization that is to rotate it away from its longitudinal thermal equilibrium $\vec{M}_0$. By doing so, the magnetization, having gained a transverse component, starts precessing and emitting signals. For an on-resonance isochromat[3] the flip angle $\theta$ obtained by an RF pulse $B_1(t)$ of duration T is given by:

$$\theta = \int_0^T \gamma B_1(t) dt \tag{3.8}$$

[3] An isochromat is a group of spins with the same precession frequency.

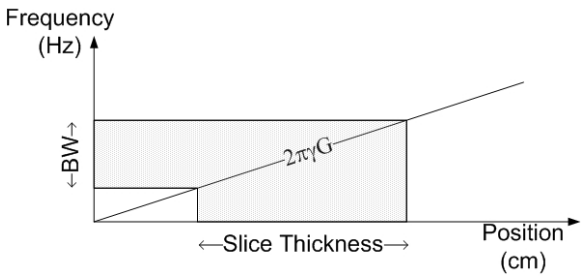


Figure 3.1: Relationship between the bandwidth (BW), the gradient (G) and the slice thickness.

When a spatially selective RF pulse is desired, a gradient is played simultaneously with $B_1(t)$. The $B_1$ frequency is also matched to the Larmor frequency at the center of the desired slice. In such case, only the spins at the center of the slice will be on-resonance. A certain bandwidth is therefore imparted to the RF pulse in order to excite a slice of a given thickness. This is done by AM modulation. For low flip angles, the envelope of the RF pulse is simply the Fourier transform of the slice profile. In such case the slice thickness is related to the bandwidth (BW) by:

$$BW = 2\pi\gamma G * SliceThickness \tag{3.9}$$

This relationship is illustrated in Fig. 3.1.

More generally, for small tip angles, the RF energy deposited in k-space can be seen as the Fourier transform of the magnetization profile(4). Multi-dimensional magnetization profiles can thus be designed using this method. For higher flip angles ($160^\circ$ and above) the linearity assumption doesn't hold. Having a given RF waveform, it is easy to perform a Bloch simulation to generate the magnetization profile but it is harder to design the waveform based on the desired profile. Another problem is the fact that null phase magnetization profile can't be obtained with finite energy. In some cases it is necessary

to obtain a roughly linear phase such that it can be rephased using gradients. In those cases, methods such as optimal control(5) or Shinnar-Leroux transform (SLR)(6) can be used. These methods allow generating RF pulses based on design parameters such as total energy, magnetization profile phase, pass band and stop band acceptable error, etc.

## 3.4 Steady State:

Steady state magnetization can occur after repeated excitation when TR is in the order of $T_1$ or $T_2$. At thermodynamic equilibrium (Fig. 3.2 A), longitudinal and transverse magnetizations are given by:

$$M_z(0^-) = M_0 \tag{3.10}$$

$$M_{xy}(0^-) = 0 \tag{3.11}$$

After a first excitation with tip angle $\alpha$ (Fig. 3.2 B) the magnetization becomes:

$$M_z(0^+) = M_0 cos(\alpha) \tag{3.12}$$

$$M_{xy}(0^+) = M_0 sin(\alpha) \tag{3.13}$$

Transverse magnetization $M_{xy}$ decays towards 0 with time constant T2 while longitudinal magnetization $M_z$ recovers towards $M_0$ with time constant T1. Mxy is then spoiled before the next excitation. Spoiling is either done by changing the RF phase quadratically or by adding a large gradient varying pseudo-randomly between TRs. After a finite number of excitations, the magnetization reaches a steady state. Before reaching steady state, signal decreases progressively which can lead to inconsistent amplitude in k-space.

The Ernst angle is the theoretical tip angle maximizing the transverse magnetization (and thus SNR) in the steady state:

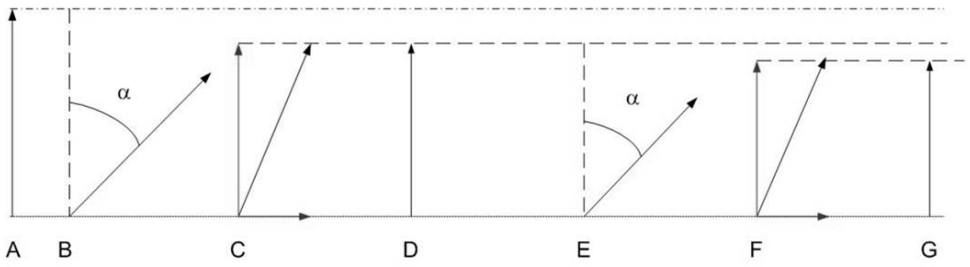


Figure 3.2: Approach to steady state. A) t=0- before the first excitation, longitudinal magnetization is at equilibrium. B) t=0+: $\alpha^{\circ}$ excitation. C) Longitudinal magnetization recovers D) t=TR- transverse magnetization is spoiled. Repeated for E, F, and G.

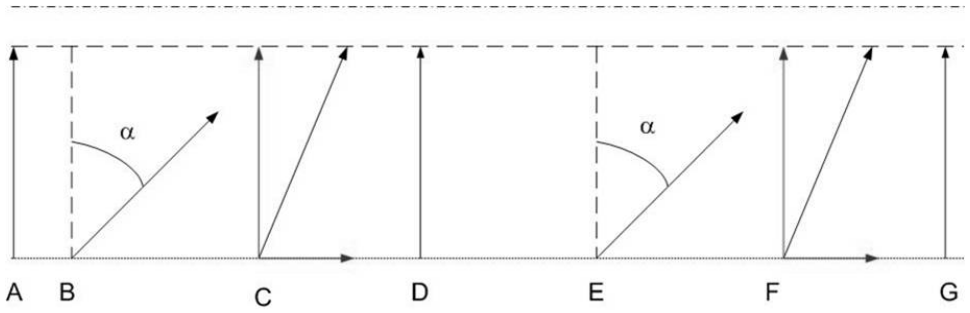


Figure 3.3: Steady state. A) t=nTR- before the $n^{th}$ excitation, longitudinal magnetization is below equilibrium. B) t=TR+:$\alpha^{\circ}$ excitation. C) Longitudinal magnetization recovers until its equal to the one in A D) t=(n+1)TR- transverse magnetization is spoiled. Repeated for E, F, and G.

$$cos\alpha = e^{-TR-T1} \tag{3.14}$$

Higher flip angles can however be used to improve the T1 contrast.

## 3.5 Introduction to k-space Sampling And Trajectory Design

Concept of k-space was proposed by Ljunggren *et al.* (7) as a way to represent the Fourier pair of the image domain and its sampling. Defining the position in k-space as a function of the area under the gradients:

$$\vec{k} = \begin{cases} k_x(t) = \hat{\gamma} \int_0^t G_x(\tau) d\tau \\ k_y(t) = \hat{\gamma} \int_0^t G_y(\tau) d\tau \\ k_z(t) = \hat{\gamma} \int_0^t G_z(\tau) d\tau \end{cases} \tag{3.15}$$

The signal $s(t)$ measured by the antennas can be written:

$$s(t) = \iiint_{xyz} M(x, y, z) e^{-i2\pi(k_x(t)x + k_y(t)y + k_z(t)z} dz dy dx \tag{3.16}$$

Which can be seen as a Fourier transform of the magnetization $M(x, y, z)$ to be reconstructed. The sampling of k-space is traditionally explained by distinguishing frequency and phase encoding. This is because in Cartesian imaging frequency and phase encoding are typically decoupled by axis (say frequency encoding on $kx$ and phase encoding on $ky$). The distinction becomes blurrier with non-Cartesian imaging. There, the concept of k-space trajectory is more informative. In its most basic essence, the concept of trajectory can be presented as a way to efficiently sample a 2D plane or 3D volume at (or above) the Nyquist criterion using a series of readouts. The trajectory can also undersample k-space in parts or in totality. This is done when the missing k-space data can be inferred using parallel imaging or compressed sensing or as a trade-off between undersampling artifacts and acquisition time. The readouts can be rectilinear as in Cartesian imaging but do not need to be. Trajectory design is as much an art as a science. The properties of a given trajectory depend on several factors including sampling efficiency, readout duration, point spread function, sensitivity to system imperfections and 0th moment at the origin. Trajectories are also subject to system and physiological restrictions such as maximum gradient, maximum slew rate (define), maximum SAR (define) as well as other heating and duty cycle limitations.

*Gradient Limitations*

Gradients are limited by amplitude ( 40 mT/m or 4 G/cm) and by their rate of change or slew rate ( 150T/m/s). This limit is set to system performance limitations and/or to physiological restrictions. In practice, these limitations mean that k-space trajectories have limited speeds and curvature speeds.

*Readout duration*

The choice of the readout duration is often a trade-off between sensitivity to susceptibility artifacts and sampling efficiency. Indeed, the longer the readout, the more spurious phase accrual. The nefariousness of this spurious phase depends on the speed at which k-space is traversed and the geometry of the trajectory. For trajectories that move rapidly through k-space, the effect of the spurious phase will be lower relative to the spatial encoding phase. For Cartesian scans that read a single k-space line per readout, off-resonance effects will be limited to a spatial shift of the off-resonance spins. Suppose that a local voxel is off-resonance due to a spurious gradient $G'x$. The spatial encoding phase during the application of a constant Cartesian readout gradient $Gx$ will be given (8) by:

$$\phi(t) = -2\pi\hat{\gamma}(G_x x + G'_x x)t \tag{3.17}$$

$$\phi(t') = -2\pi k_x x(1 + G'_x/G_x) \tag{3.18}$$

The apparent coordinate x' of the voxel will therefore be related to the actual coordinate x by :

$$x' = x(1 + G'_x/G_x) \tag{3.19}$$

We see that the higher the magnitude of the readout gradient, the smaller the distortion. This is because for a given k-space coverage the magnitude of the readout gradient is inversely proportional to the readout time, just as speed is inversely proportional to distance covered. Although the previous discussion focused on off-resonance due to spurious susceptibility induced gradients, the same analysis can be done for chemical shift induced off-resonance.

The effect of off-resonance on non-Cartesian scans is more complicated and will be covered in details in Chapter 6.

*Gradient Moments and Flow Compensation*

The $n^{th}$ moment of a gradient is defined as:

$$m_n(t) = \int_o^t G(u)u^n du \tag{3.20}$$

To desensitize sequences to flow, nulling low order moments is especially important in the center of k-space where most of the image energy is located. Sequences in which the readout starts at the center of k-space (eg. spiral-out) have better flow properties than those that have large 0th moments at the origin.

*Eddy currents*

Eddy currents are spurious magnetic fields induced by the switching of gradients and their coupling with large conductive structures inside the magnet. Eddy currents result in undesirable time varying (and potentially spatially varying) gradients that are detrimental to imaging. Their effects is usually less pronounced in Cartesian imaging where the apparent gradient delay often caused by eddy currents results in a simple k-space shift. As a general rule, pulse sequences that employ high slew rates are more prone to errors caused by eddy currents.

## 3.6 Introduction to Image Reconstruction

*Cartesian vs. Non-Cartesian sampling*

MRI acquisitions sample k-space which is the Fourier transform of the image. Cartesian sampling measures k-space on a regularly spaced rectilinear grid which is directly Fourier transformed. These acquisitions have many desirable properties such as :

1. Fast and simple reconstruction ($FFT^{-1}$)
2. No noise coloring due to non-uniform sampling
3. Well understood Nyquist sampling criterion that can be met exactly
4. Simple and well behaved point spread function (PSF)
5. Resolution is easily defined and determined.

This simplicity is reflected in the wide-spread use of Cartesian sampling in routine clinical imaging. Many promising applications, however, require non-Cartesian sampling. A large body of work has illustrated the potential benefits of various non-Cartesian methods (such as, radial, spiral, etc.) in a variety of applications. In the past decade PROPELLER, a non-Cartesian method has even managed to become the gold standard in some clinical neuroimaging applications. Advantages of non-Cartesian methods may include:

1. Scan efficiency
2. Robustness against motion
3. Insensitivity to flow
4. Ability to image with very short TE

5. Design flexibility

*Reconstructing non-Cartesian data*

Since the inverse FFT can only be performed on Cartesian data, it is necessary to first interpolate the non-Cartesian data onto the Cartesian grid points. This process is called gridding. The most reliable and widely used non-Cartesian reconstruction strategy will be referred to as "Conventional Gridding"(9). Other methods also exist, including the Non-Uniform Fourier Transform (NUFFT (10)) which is equivalent to conventional gridding, the Uniform ReSampling method-URS (11) and its variants URS (11, 12) which can be made faster than gridding but are less reliable.

*Conventional gridding reconstruction*

The non-Cartesian points are first multiplied by a sampling compensation weighting and smeared onto Cartesian points using a convolution kernel. The gridded k-space can then be inverse Fourier transformed to image space. Finally, the low pass filtering effect of the smearing is removed by dividing the image by a rolloff function which corresponds to the inverse Fourier transform of the gridding kernel(9). For conventional gridding reconstruction, this is typically estimated using four steps.

1. Sampling Density Compensation (SDC)

2. Interpolating the data onto a Cartesian grid by convolution

3. Fourier transforming the data

4. Applying a rolloff correction filter to high-pass filter k-space

The selection of a gridding convolving function depends on two parameters, the grid oversampling ratio and the kernel width, that can be used to trade

accuracy for computational memory and time reductions. The optimal convolution function is an infinite sinc(13), but this function is computationally impractical. Any finite convolution function will contribute side lobes which will be aliased back into the image by convolution with the "shah" function. The Kaiser-Bessel has been found to be the most practical convolution kernel in terms of amplitude and placement of the aliasing side lobes, as well as ease of computation (9).

Substantial reductions in computation memory and time can be obtained while maintaining high accuracy by using a minimal oversampling ratio, from 1.123 to 1.375, instead of the typically employed by grid oversampling ratio of 2 and by pre-sampling the Kaiser-Bessel kernel(14).

If the gridding is done properly, the quality of the resulting image depends mainly on the sampling density compensation (SDC) function used. Substantial profile distortion may appear if the SDC is not optimized.

# Chapter 4

## 3D PROPELLER-BASED DIFFUSION WEIGHTED IMAGING

Diffusion sensitized MRI pulse sequences are used to image the amount and preferential directions of diffusion in tissues(15). Clinically, Diffusion Weighted Imaging (DWI) is mainly used to detect and evaluate the extent of brain stroke. Although rarely done clinically, white matter integrity and fiber tracking information can also be obtained using diffusion imaging sequences. Diffusion Tensor Imaging (DTI) and Diffusion Spectrum Imaging (DSI) are among such promising schemes. Although all MRI pulse sequences are somewhat sensitive to diffusion, additional diffusion sensitizing gradients need to be added after excitation to make them diagnostically useful. These gradients have the disadvantage of also sensitizing the sequence to bulk motion.

The common way to deal with motion phase is simply to acquire the full k-space in a single-shot. The advantage of single-shot methods is that motion phase can be discarded in image space. This is because there is no need to combine the data from multiple excitations. One problem with single-shot methods is the need for long acquisition windows. Spins that are off resonance due to local magnetic susceptibility differences will have time to accrue substantial amounts of phase during this period. This leads to severe artifacts, distortion and signal loss. Another problem is the limitation of single-shot methods to low resolution imaging. There is simply not enough time to acquire a full-FOV, high-resolution image within a single acquisition window.

There are two main types of commonly used diffusion sequences: Echo Planar (EPI) based and Fast Spin Echo (FSE) based. Typical EPI methods sample the whole 2D k-space in a single-shot whereas FSE methods are typically multi-shot. Multi-shot methods based on Steady State Free Precession (SSFP)

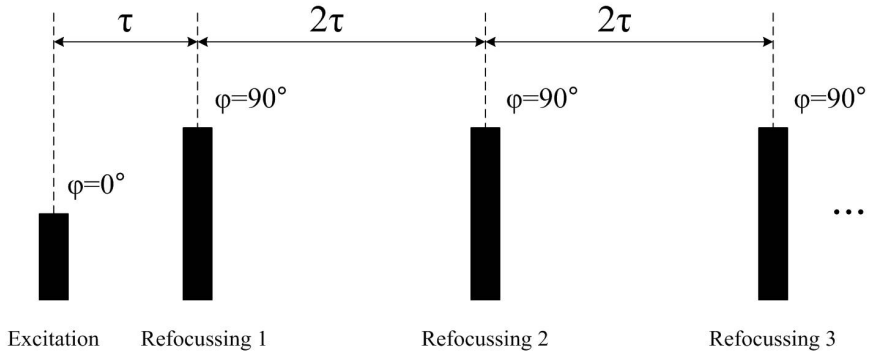


Figure 4.1: The CPMG RF pulse train

sequences have also appeared in the literature (16) but are controversial due to the "multi pathway" nature of their magnetization signal.

## 4.1 Spin Echo Trains

Spin echo trains pulse sequences such as Fast Spin Echo (FSE) are often used to reduce the scan time of spin echo signal acquisitions. Assuming no motion and time-constant field inhomogeneities, a stable echo train can theoretically be obtained by a series of perfect $180^\circ$ refocusing pulses around arbitrary axes in the transverse plane. The stability of the signal obtained by such train is only limited by the T2 signal decay. The main practical limitation of such method resides in the flip angle requirement. Indeed there are applications in which a $180^\circ$ flip angle is undesirable and/or hard to obtain consistently over the imaged volume. The main factors limiting flip angles are Specific Absorption Rate (SAR), Magnetization Transfer (MT) effects and B1 inhomogeneity, all of which become especially problematic at 3T and above. In T2 weighted FSE sequences, CPMG (Carr-Purcell-Meiboom-Gill) echo trains are typically used to maintain signal stability in the presence of lower refocusing angles.

Imperfect refocusing pulses can be thought to decompose the magnetization in several distinct "echo pathways" (17, 18). Part of the transverse mag-

netization is perfectly refocused, part is left untouched and part is rotated to the longitudinal axis. Similarly, part of the longitudinal magnetization is excited, part is left untouched and part is inverted. The CPMG conditions is a set of conditions that, when met, ensure that the echoes produced by these pathways (primary and stimulated echoes) happen simultaneously with coherent phase. The so-called "CPMG echo trains" thus obtained maintain signal stability in the presence of lower refocusing angles. In the case of FSE sequences, the CPMG conditions can be reduced to 2 conditions. The first condition requires the sequence to be played according to the timing and RF phase scheme described in Fig. 4.1. The second condition dictates that all spins must accumulate the same phase between any two consecutive refocusing RF pulses. This means that the sequence must come back to the same k-space location before every refocusing RF pulse. When these conditions are met, primary and stimulated echoes occur at the same point (between the refocusing pulses) and add coherently. As mentioned earlier, the application of diffusion gradients after the excitation makes the average spin phase very sensitive to bulk motion of the patient. Even slight movements and physiological pulsations result in large phase increments that will not be refocused since they are not due to differences in their constant precession frequencies. For diffusion imaging therefore, the CPMG conditions are not met. In such case, more complicated schemes must be used in order to have a stable echo train. Either the non-CPMG component must be eliminated or non-CPMG phase cycling methods must be employed to dictate the phases of the RF refocusing pulses.

If a CPMG echo train is used in such condition, the in-plane magnetization component that is parallel to the refocusing pulse phase (MG component) will be stable but the perpendicular component (non-MG component) will rapidly

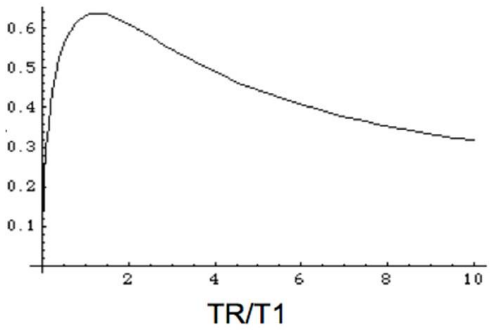


Figure 4.2: Approximate time-normalized SNR for a DWI sequence

decay to 0. This causes 2 main issues. In addition to losing roughly half of the signal, this loss varies greatly from echo to echo which causes potential streaking artifacts in the reconstructed image. To mitigate this problem it is preferable to first crush the perpendicular component before the CPMG refocusing pulse train(19). Half of the signal amplitude is lost but the remaining signal thus obtained is much more stable. Another approach to avoid this phase dependent decay is to alter the phase of the refocusing RF pulses so that both in-plane components will, in turn, be somewhat rephrased. Phase cycling schemes such as MLEV and XY(20–22) have thus been adopted from the NMR literature to help slightly relax the flip angle requirement. However, the stability obtained still breaks down when the flip angle strays too far from $180°$. An improved phase cycling scheme was developed by Patrick LeRoux(23) which further improves the echo train stability even when the flip angle is as low as $120°$.

## 4.2 Time-Normalized SNR Optimality

To obtain full brain coverage, FSE-based DWI sequences such as DW-PROPELLER typically employ a slice interleaving scheme. At every TR period a given slice is excited and a portion of its k-space is sampled. Then a recovery period is required for the magnetization in the slice. During that time other slices can be

sampled. The first 50ms after excitation ($t_{diff}$) are used for diffusion encoding during which no signal is acquired. After that period, sampling begins and a portion of k-space is traversed during a period ($t_{ADC}$). The sampled signal strength decays with t as $e^{-t/T2}$. There is therefore a SNR trade-off between few, long acquisitions of a decaying signal and frequent, short acquisitions of a relatively strong signal. SNR can always be improved by increasing the total sequence duration.

$$SNR \propto \sqrt{sequencetime} \tag{4.1}$$

Therefore, a measure of SNR optimality for a given sequence needs to be time normalized.

$$SNR^* \propto SNR/\sqrt{sequencetime} \tag{4.2}$$

The lower bound of Equation 3 is optimal for FSE sequences where excessive RF energy deposition is not an issue.

$$TR \geq (t_{diff} + t_{ADC}) * N_{slices} \tag{4.3}$$

Without considering image artifacts, one can calculate how long the acquisition period should be for time-normalized SNR optimality.

$$SNR \propto e^{-TR/T1} \int_{t_{diff}}^{t_{diff}+t_{ADC}} e^{-t/T2} dt \tag{4.4}$$

In brain imaging, the tissues of interest have a T1 in the order of 1s and a T2 in the order of 100ms. An approximate calculation of the time normalized SNR is shown on Fig. 4.2. In practice, this figure indicates that the TR should be the 1-2 second range. To have such a short TR, an FSE sequence should partition full brain coverage ( 14cm in height) in 10-20 slabs. This is far from

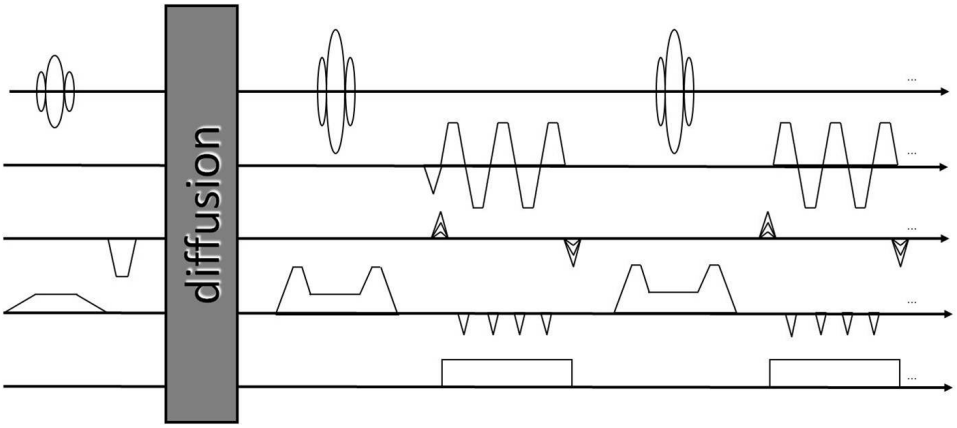


Figure 4.3: The ROTOR pulse sequence diagram. From top to bottom axes show RF, Gx, Gy, Gz, and ADC.

the 70 slices needed for full coverage with traditional multislice DW FSE. The ROTOR method proposed in this work does away with fewer, thicker slabs by phase encoding them in the slab direction.

## 4.3 Methods

The ROTOR trajectory is based on the Turboprop sequence(24, 25) where the gradient echoes are placed in the slab encoding direction (Fig. 4.3). The slab selective blades (Fig. 4.4, Table 1) spiral down in (kx, ky, z) space (Fig. 4.5). Custom SLR(6) RF pulses are employed to obtain sharp slab boundaries. Slab boundary artifacts are further mitigated by sliding the encoded slab down progressively in z as the blade rotates in kx,ky (Fig. 4.5). The kz encoding positions are spaced by (1/slab thickness) instead of (1/FOV), greatly increasing the speed of the kz trajectory, thus minimizing warping by factors of 20 compared to fully sampled FOV EPI. The slab encoding gradient is matched to the average of a kz blip over a readout period; this eliminates bent slabs in regions of off-resonance. To avoid aliasing in the slab direction, kz encoding is over-sampled and the extra z locations are discarded.

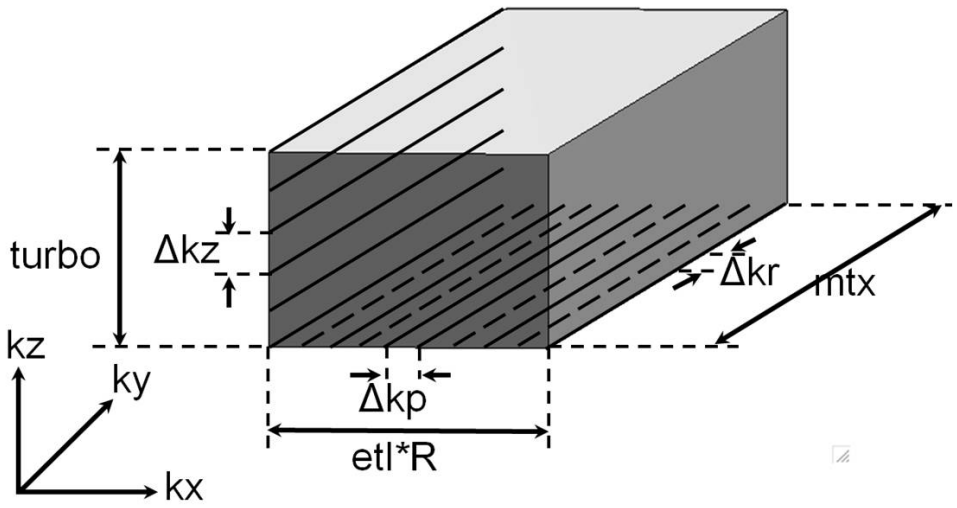


Figure 4.4: The ROTOR blade dimensions

Table 4.1: ROTOR Parameters definitions

| Parameter | Description |
|---|---|
| etl | Nb. spin echoes per excitation |
| turbo | Nb. gradient echoes per spin echo |
| R | GRAPPA acceleration factor |
| mtx | Nb. data points per readout |
| Δkr | Dist. between readout points. Equals $FOV^{-1}$ |
| Δkp | Dist. between non-accelerated phase encoded lines. Equals $FOV^{-1}$ |
| Δkz | Dist. between data points in kz. Equals $(s+)^{-1}$ |
| s | Excited slab thickness |
| s+ | Extent of the spatially resolved slab thickness |

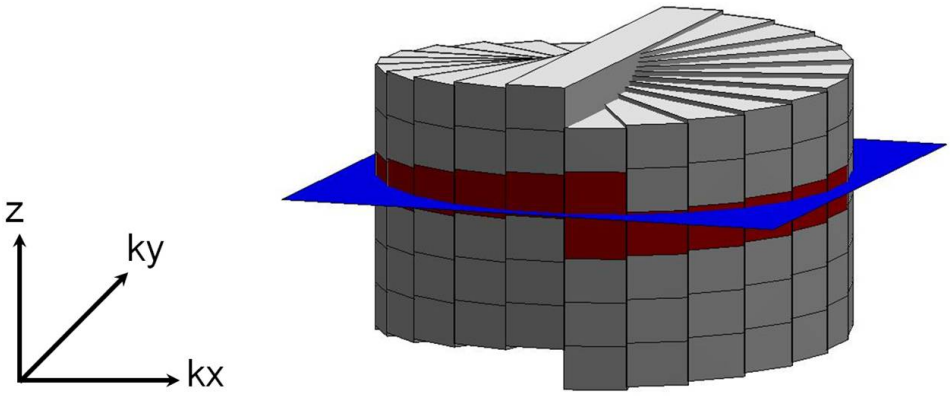


Figure 4.5: A blade in (kx, ky, z) space showing the sliding slab scheme. The blades in red contribute to the plane in blue during gridding.

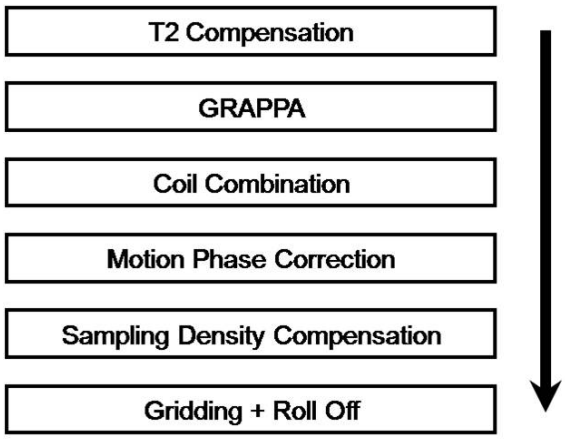


Figure 4.6: The ROTOR image reconstruction pipeline

The non-CPMG echo-train stability was improved by Le Roux phase cycling (23). The reconstruction pipeline is described in (Fig. 4.6). Separate calibration scans are used to train the parallel imaging GRAPPA(2) weights. After GRAPPA, coil combination is performed separately for odd and even echoes(24). Linear in-plane motion phase (corresponding to shifts in k-space) is added back to the phase-corrected blade images. The blades are then gridded at their proper locations based upon their estimated linear motion phase.

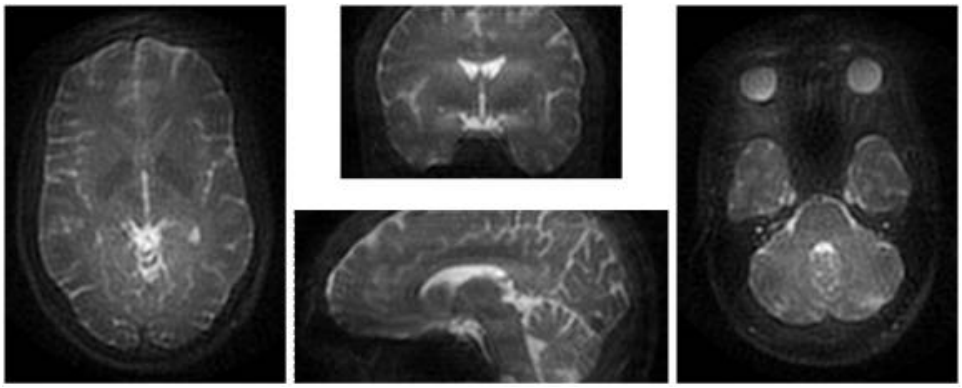

Figure 4.7: b=0 slices

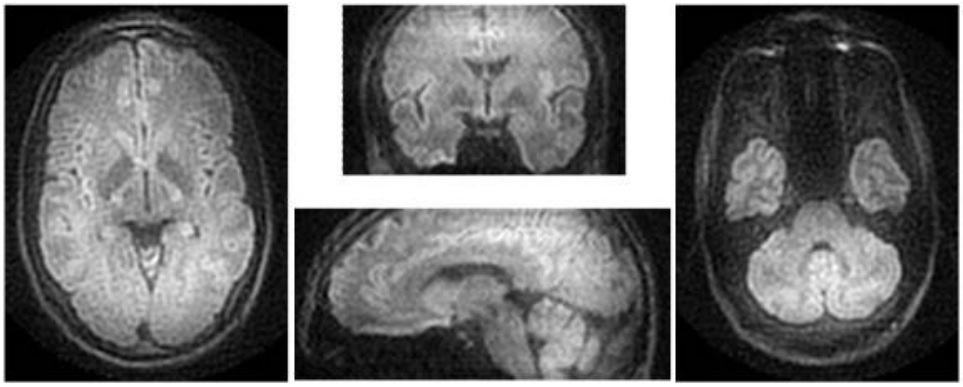

Figure 4.8: Combined DWI slices

## 4.4 Experimentations and Results

A 6' DW scan of a healthy volunteer[1] was acquired with 3+1 diffusion directions on a GE SIGNA 3T scanner with an 8-channel brain coil. The volume covered was 220x220x104 $mm^3$ with a resolution of 2x2x2 $mm^3$. The imaging parameters were b =1000, TR=1.5s, NSA =6, etl =8, turbo = 7, with a slab oversampling ratio of 7/5. Fig. 4.7 shows slices of the acquired 3D volume with b=0 and Fig. 4.7, slices of the combined DWI volume.

[1]Human research done under IRB#96RA057.

## 4.5 Discussion and Conclusion

A 3D PROPELLER-based DWI pulse sequence has been developed and tested. Advantages of the method include reduced off-resonance artifacts (vs. EPI), lower SAR (vs. PROPELLER), higher SNR efficiency (vs. PROPELLER), 3D phase correction and 3D continuity. Besides DWI, other potential applications of the method include DTI and T2 weighted imaging. The technique is currently limited by the significant streaking caused by T2 decay. This is less of an issue in T2 imaging where the CPMG compliance allows for flip angle progression, thus flattening the T2 decay profile. Possible ways to mitigate this problem is to use U-FLARE, or SPLICE with tailored flip angles (26). These methods separate the echoes having been refocussed an even number of times from the ones having been refocussed an odd number of times (a.k.a. even/odd parity). These echoes having opposite phase, they usually cancel each other out, leading to signal decay. By acquiring even and odd echoes sequencially, small flip angles can be used without risk of losing echo train stability. The SPLICE odd/even parity separation is illustrated in Figs. 4.9 and 4.10. Caveats to consider are the $\sqrt{2}$ penality in SNR incured and the possible sensitivity of the T2 decay profile to $B_1$ homogeneity.

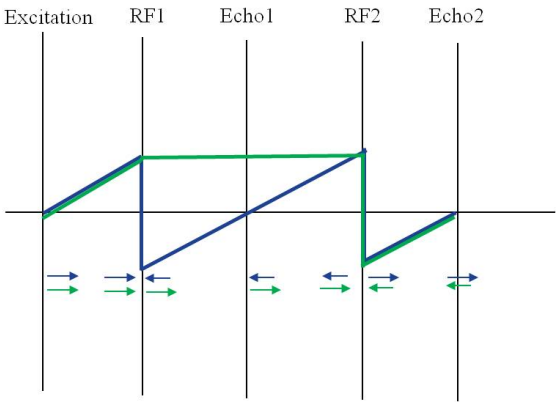


Figure 4.9: In the CPMG sequence, when a non-MG component is present, the sign of this component flips when refocused. The green echo pathway in this example undergoes 1 fewer refocussing event and ends up with a phase that is opposite to the phase of the main pathway (blue) at the time of echo 2. Phase reversal is illustrated by the direction of the arrows.

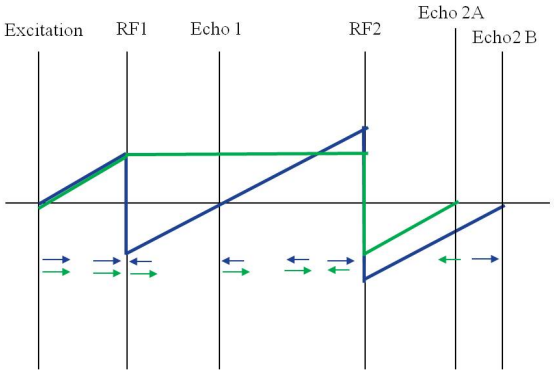


Figure 4.10: Splice separates the echoes from the different echo pathways so that they do not add destrcutively. Phase reversal is illustrated by the direction of the arrows. More detailed explanations can be found in (26).

# Chapter 5

# PRACTICAL ORTHOGONAL BRAIN SCANS FOR CLINICAL ENVIRONMENTS

## 5.1 Introduction

Three dimensional brain scans such as T1W SPoiled GRadient Echo (SPGR) are commonly used when it is desirable to look at a volume in two or three orthogonal orientations (e.g. axial, sagittal and coronal). In addition to relatively long scan durations, such acquisitions suffer from long exam reading time. This is due to the large number of images to read and compounded by their low SNR. In theory, this should not be an issue since 3D acquisitions can be reformatted into thick slices, thus reducing the number of images and improving SNR. While this is indeed the preferred way of looking at these datasets, these scans remain tedious to read in practice. This is due to many radiologists belief that they are obligated to review any reconstructed image regardless of their low added diagnostic value. Another drawback of typical 3D acquisitions is their practical inefficiency: radiologists rarely look at reconstructed cuts oblique to the original prescription. This means that a large proportion of the data acquired in 3D acquisitions will never be used when looking at reformatted slices. The aim of this paper is to offer a fast, high SNR scan with high in-plane resolution but low through-plane resolution in all relevant orientations.

## 5.2 Methods

A fraction of the full 3D Cartesian k-space is sampled in 3 subsets (eg. axial, sagittal and coronal) having high in-plane resolution but low through-plane resolution (Fig. 1a). All subsets are acquired following identical 3D excitations in

the z (I/S)[1] direction. This helps reduce the minimum z FOV to be prescribed. Each subset is accelerated using parallel imaging. Design choices regarding parallel imaging were made based on two assumptions: 1) the typical head coil geometry does not allow parallel imaging acceleration in the z (I/S) direction and 2) it is most efficient to readout in a direction of high resolution and large FOV. Based on the typical brain exam dimensions presented in Table 5.1, this makes the ky, ky and kx directions optimal for readout of the axial, sagittal and coronal sets, respectively. The acceleration directions of the axial, sagittal and coronal sets are therefore kx, kx and ky, respectively. This acquisition scheme is further detailed in Fig. 1 and Table 5.2. The intersection between the axial and sagittal sets (yellow region in Fig. 1a) allows for training of both the kx and ky GRAPPA kernels (Fig. 1e). Only ky readouts are thus used for calibration. This avoids calibration errors due to misregistration of k-space points caused by readout delays. The prescription frame can be slightly rotated (e.g. to match the A/P direction with the main axis of the frontal lobe) without substantially affecting this imaging scheme.

## 5.3 Experimentations and Results

A multi-resolution dataset was synthesized from two fully sampled SPGR datasets. Dataset A, from which the axial and sagittal multi-resolution subsets were extracted, had its readout direction in ky. Dataset B, from which was generated the coronal subset, had its readout in kx. Datasets were acquired from a healthy volunteer on a GE SIGNA 3T scanner with an 8-channel brain coil. The volume covered was 175x230x154 $mm^3$ with a matrix of 288x384x256 for dataset A and 288x48x256 for B. The imaging parameters were: TR=10.1ms, Flip Angle=12°,

[1]The DICOM coordinate convention will be used throughout this paper. Right to Left (L/R) corresponds to the +x direction, Anterior to Posterior (A/P) to +y and Inferior to Superior (I/S) to +z.

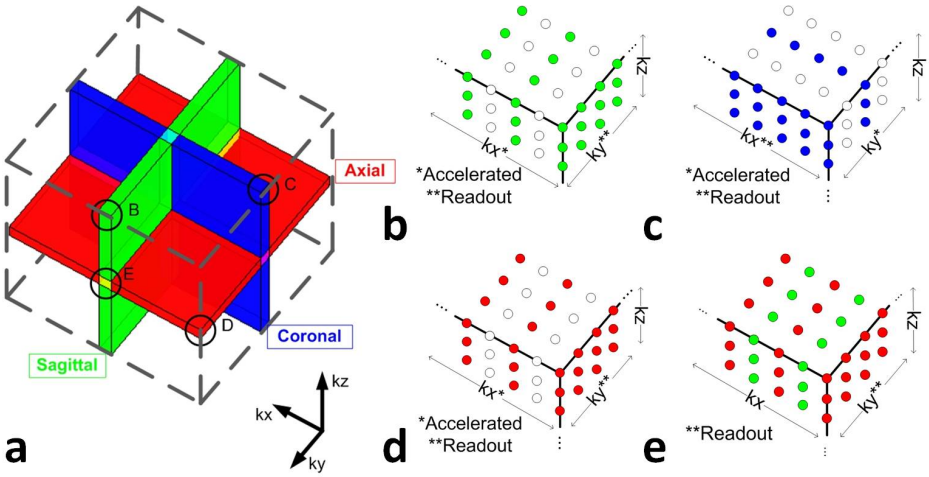


Figure 5.1: Accelerating the 3D Multi-resolution dataset. Red data points are acquired by the sagittal set, blue ones by the coronal set, green ones by the sagittal set and white data points are never acquired. a: The multi-resolution scheme proposed. The dashed gray lines delineate the k-space volume filled in typical 3D Cartesian acquisitions. The circled areas B-E are detailed in Fig 1 b-e. b-d: Sagittal, coronal and axial accelerations, respectively e: the GRAPPA training set.

BW=31.25 kHz, NSA=1. The multi-resolution subsets were downsampled according to the specifications provided in Table 5.2. The total acquisition time of the multi-resolution set would have been 2m25s versus 12m29s for the fully sampled set A. Dataset A' was obtained by accelerating A in kx with R=2 resulting in a required scan time of 6m20s including autocalibration lines. Slices from the multi-resolution set were compared with reformatted cuts from A and A'. The reformatting was performed by arithmetic averaging of 8 consecutive slices, thus resulting in an identical through-plane resolution as for the multi-resolution images. Image comparisons are presented in Fig. 2. The theoretical relative SNR of each slice was calculated as:

$$\frac{SNR_A}{SNR_B} = \frac{\sqrt{SD_A}}{\sqrt{SD_B}} * \frac{V_A}{V_B} * \frac{\sqrt{NA_A}}{\sqrt{NA_B}} \tag{5.1}$$

Table 5.1: Imaging parameters for the full 3D SPGR set A

| | x (L/R) | y (A/P) | z (I/S) |
|---|---|---|---|
| FOV | 175mm | 230mm | 154mm |
| Matrix Size | 288 | 384 | 256 |
| Voxel Size | 0.6mm | 0.6mm | 0.6mm |

Table 5.2: Imaging parameters for the multi-resolution set

| | x (L/R) | y (A/P) | z (I/S) |
|---|---|---|---|
| Readout | ky (A/P) | ky (A/P) | kx (L/R) |
| Acceleration | kx (L/R) | kx (L/R) | ky (A/P) |
| Slices | kz (I/S) | kx (L/R) | ky (A/P) |
| Excitation | z (I/S) | z (I/S) | z (I/S) |
| Number of Slices | 32 | 36* | 48* |
| In-plane Matrix Size | 288*x384 | 384x256 | 288x256 |
| In-plane Voxel Dimension | 0.6x0.6mm$^2$ | 0.6x0.6mm$^2$ | 0.6x0.6mm$^2$ |
| Through-Plane Voxel Dimension | 4.8mm | 4.8mm | 4.8mm |
| Acquisition Time** | 47s | 36s | 62s |

*With factor R=2 acceleration.
**With TR=10.1ms.

Where SD is the total scan duration, V is the volume of a voxel and NA is the number of voxels averaged together during reformatting. For instance, the relative SNR of the coronal image obtained with the proposed method vs. the GRAPPA accelerated Cartesian set A' is given by:

$$\frac{SNR_{proposed}}{SNR_{A'}} = \frac{\sqrt{62'}}{\sqrt{380'}} * \frac{8}{1} * \frac{\sqrt{1}}{\sqrt{8}} = 1.14 \tag{5.2}$$

Relative SNR comparisons are presented in Fig 5.2.

## 5.4 Discussion

Fig. 2 suggests that the proposed method results in slices of roughly comparable image quality to a GRAPPA accelerated acquisition reformatted to identical through-plane resolution while comparing advantageously in terms of scan duration (2m25s vs. 6m20s). More importantly, the proposed method does not

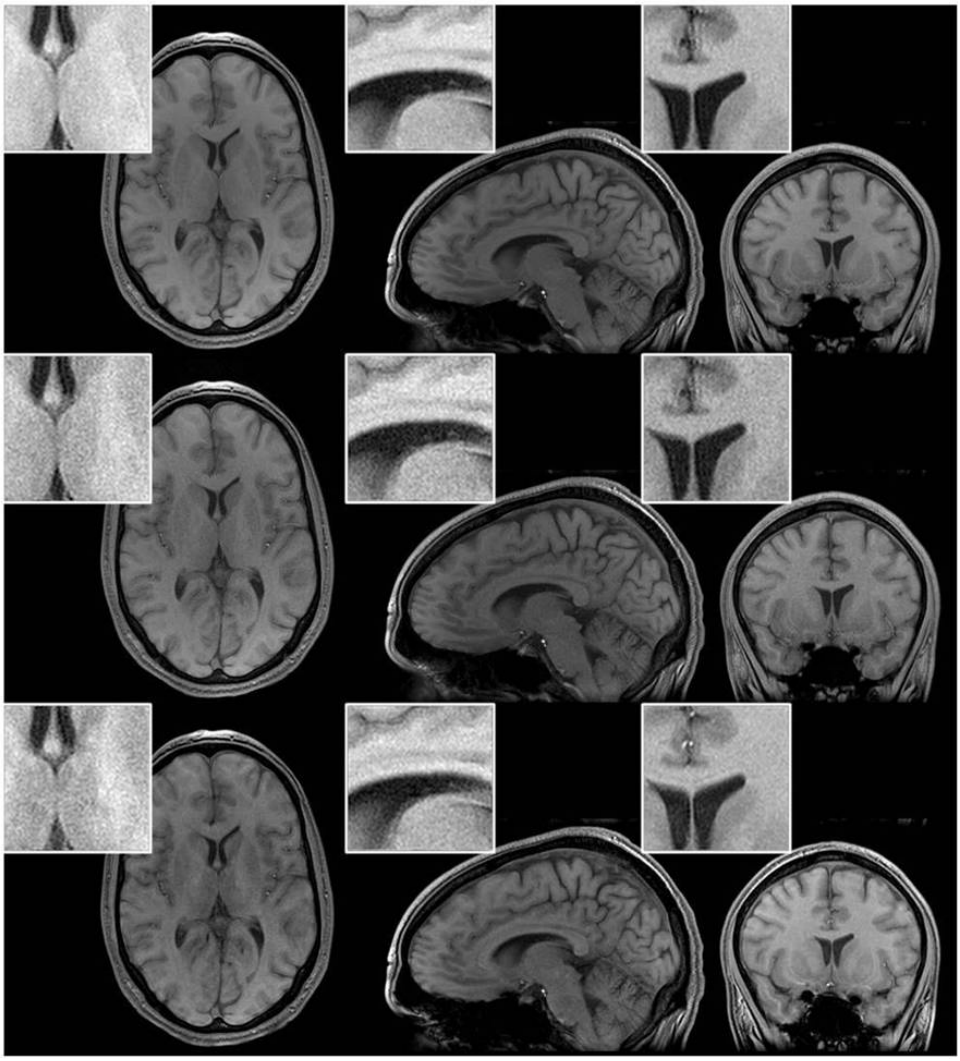

Figure 5.2: Slice comparisons. Reformatted full Cartesian set A with acquisition time 12m29s (top), reformatted GRAPPA accelerated Cartesian set A' with acquisition time 6m20s and proposed method with acquisition time 2m25s (bottom). Axial images (left) have matrix size 288x384, sagittal (middle) 384x256 and coronal (right) 288x256. All images have in-plane resolution 0.6x0.6$mm^2$ and through-plane resolution 4.8mm. The axial, sagittal and coronal relative SNR of the proposed method are .70, .62 and .81 respectively when compared to the reformatted full Cartesian and .98, .87 and 1.14 when compared to the reformatted GRAPPA accelerated Cartesian set A'.

involve the reconstruction of a large number of low SNR images. These factors yield image sets with a clinically practical number of slices in three orthogonal planes and result in a lower total scan cost.

# Chapter 6

# ITERATIVE DEBLURRING OF SPIRAL IMAGES

## 6.1 Motivation

It has been shown(27) that for gradient echo sequences, the relative SNR per spin (leaving voxel size and T1 contrast unchanged) follows:

$$SNR_{spin} \propto \sqrt{T}\sqrt{\tau} \tag{6.1}$$

Where $\tau$ is the is the duration of the sampling period and $T$ is the scan time. Therefore, short of hardware improvements, the only way to decrease scan time without changing T1 contrast or $SNR_{spin}$ is to increase the duration of the sampling period. Such increase has the effect of sensitizing the sequence to off-resonance distortion. Spiral imaging is a trajectory that is well suited for long acquisition windows. Deblurring of these images is generally performed by making some assumption on the smoothness of the spatial $B_0$ field (28–31). In practice, off-resonance can vary rapidly in regions of susceptibility differences and in the presence of fat. Iterative methods have been proposed (32, 33) to relax the $B_0$ smoothness requirement but do not address the issue of fat and coil combination. One common way to deal with fat is to first perform a 3 point Dixon fat/water separation (34). In the presence of blurring however, a fat region can blur onto a region of significantly different image phase. Therefore, typical phase correction cannot be performed adequately even in the presence of a perfectly known field map. This work proposes an iterative approach to deblurring with or without fat separation.

## 6.2 Effects of off-resonance on non-Cartesian scans

As explained in chapter 3, the effect of off-resonance on Cartesian scans is a spatial shift. Because non-Cartesian imaging does not use rectilinear gradients, off-resonance voxels will be "shifted" differently in different parts of k-

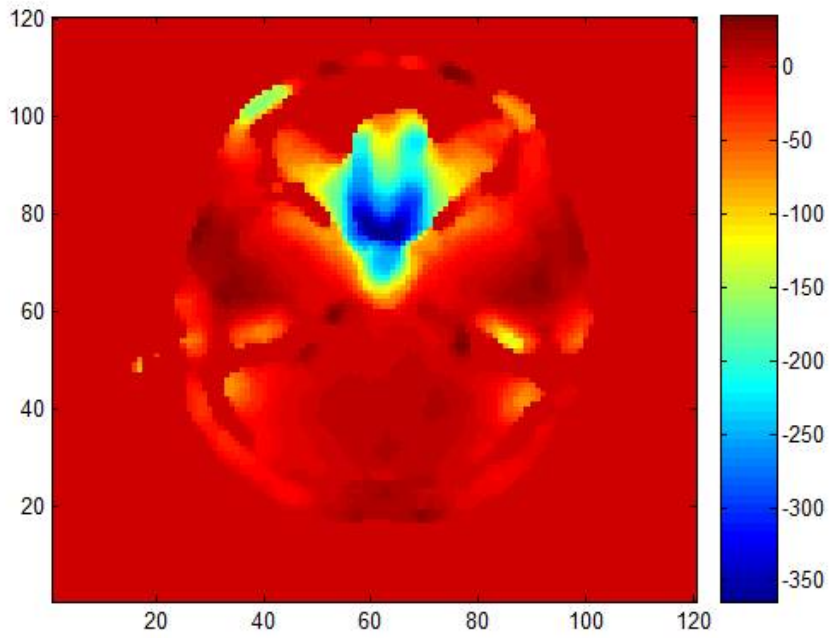


Figure 6.1: Smoothed off-resonance map $\Delta(x, y)$ in Hertz.

space. This will lead to a blurring rather than a shift. The blurring of a given voxel depends on the local off-resonance $\Delta(x, y)$ it is subject to. Off-resonance maps are usually obtained by acquiring images of limited resolution and short $\tau$ at different TEs. The phase progression between the different images provides an estimation of the off-resonance. Special attention must be given to phase wrapping and to the possible presence of fat which precesses slower than water in a given field. An off-resonance map of a brain slice in a region of high susceptibility variations is presented in Fig. 6.1.

At every location, the phase $\phi$ of the local magnetization will accrue as:

$$\phi(x, y, t) = \phi_0 + 2\pi\Delta(x, y)t \tag{6.2}$$

Without loss of generality, we will assume the initial phase $\phi_0 = 0$ for now. Depending on the trajectory used, different k-space locations will be sampled at

different times after excitation. A time map curve represents the time $t$ at which a given k-space radius $k$ is sampled for a given trajectory. Substituting $t$ as $t(k)$, as found on the time map (Fig. 6.2) we obtain:

$$\phi(x, y, k) = 2\pi\Delta(x, y)t(k) \tag{6.3}$$

The circularly symetric Point Spread Function (psf) of a given voxel subject to off-resonance $\Delta(x', y')$ is therefore given by:

$$psf(x, y, x', y') = FT\{e^{-i2\pi\Delta(x',y')t(k)}\} \tag{6.4}$$

Strictly speaking, the approach presented here to represent blurring is applicable to all trajectories. In practice however, this technique is better suited for non-Cartesian trajectories that travel in k-space as a monotonic function of time. If a k-space point is sampled more than once at different time points after excitation (e.g. Lissajou trajectories), the point spread function can still be found by gridding the time at the corresponding k-space locations but the analysis will be more complicated.

## 6.3 Properties of the blurring operator

In the continuous case, the blurred image g is therefore a linear operation represented by a Fredholm integral equation of the first kind:

$$g(x, y) = \iint_{FOV} psf(x, y, x', y')f(x', y')dx'dy' \tag{6.5}$$

In the discrete case, we will write:

$$g = Bf \tag{6.6}$$

Where B is the linear blurring operator. In the general case, solving for $f$ is notoriously ill-posed problem but by making certain assumptions on the smoothness

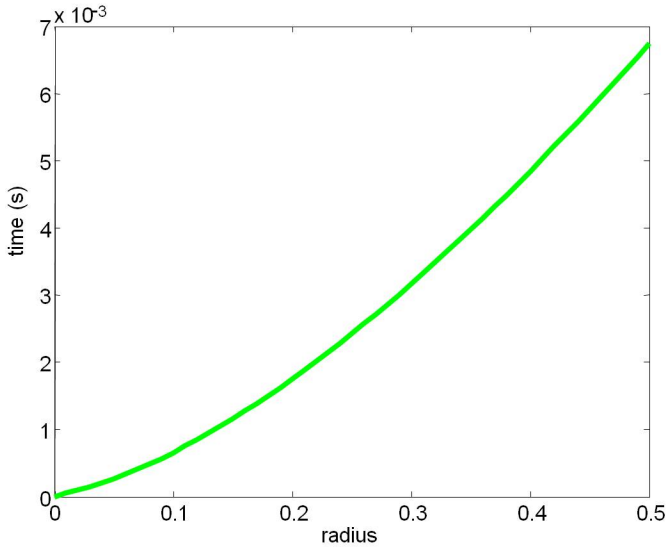


Figure 6.2: Time map of a spiral k-space trajectory with $\tau = 6.748ms$. The radius represents the distance in k-space from the origin and is measured in arbitrary units where 0.5 represents the maximum spatial frequency sampled.

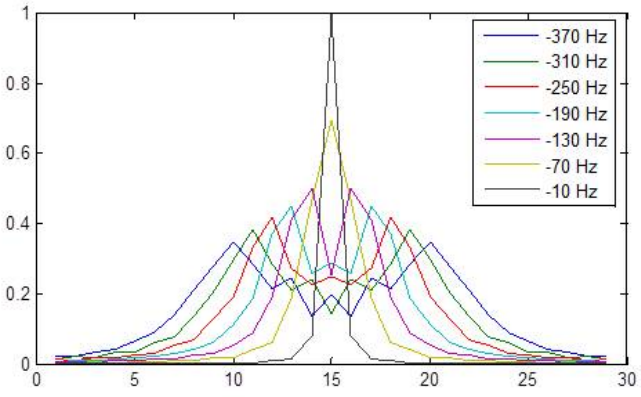


Figure 6.3: Blurring kernels for 7 different values of off-resonance found in the fieldmap of Fig. 6.1.

and magnitude of the field map $\Delta(x', y')$, it becomes tractable. Interestingly, despite the more complicated nature of blurring in non-Cartesian scans, correction of off-resonance effects on Cartesian scans is a more ill-posed problem than the deblurring non-Cartesian ones(35).

If the off-resonance is constant everywhere in the FOV (i.e. $\Delta(x, y) = \Delta$), deblurring can be performed perfectly by either *a priori* adjusting the demodulation frequency of the MR system or *a posteriori* correctiing the phase of the acquired signal $s(t)$:

$$s'(t) = s(t)e^{+i2\pi\Delta t} \tag{6.7}$$

The blurring operator B in this case is a Toeplitz matrix. By zero padding the image sufficiently, such that the blurring on one edge of the image wouldn't "wrap around" to the other side, the operator becomes a circulant matrix which means that it is diagonalized by the 2D Fourier operator. Diagonalization is an important concept to study the condition of a matrix, i.e. our ability to find its inverse. An arbitrary matrix M can always be diagonalized by the singular value decomposition:

$$M = U\Sigma V^H \tag{6.8}$$

Where $\Sigma$ is a diagonal matrix of the same dimension as M (not necessarily square) with nonnegative diagonal elements in decreasing order, and $U$ and $V$ are unitary matrices. The diagonal elements $\sigma_i$ of $\Sigma$ are called "singular values". If any of the singular values is 0, the matrix is singular and no inverse exists. If no singular value is 0, the condition number is defined as:

$$cond = ||M||||M^{-1}|| = max(|\sigma_i|)/min(|\sigma_i|) \tag{6.9}$$

The condition number of a matrix gives an indication of the accuracy of the linear equation solution. A large condition number means that the solution of a

system of linear equations is highly sensitive to errors in the data. The minimum possible condition number is 1 in which case there is no noise amplification at all. In the case $M$ is a circulant matrix, it is diagonalized by $F_{2D}$, the 2D Fourier operator:

$$M = F\Sigma F^H \tag{6.10}$$

In our case, each line of M is a circularly shifted version of the $psf$, which makes $\Sigma$ the phase function that multiplied k-space. This function has unit magnitude which means that $|\sigma_i| = 1$ and the condition number is 1. This constitutes a substantial difference between spatially invariant blurring in MRI and in other image processing fields (36).

### 6.4 Deblurring in the presence of spatially varying off-resonance

Let's define a "region of influence" around the point (x,y) by all the locations (x', y') where $psf(x, y, x', y') \neq 0$. Now assume that the field map varies slowly and is limited in magnitude such that $\Delta(x, y) \approx \Delta(x', y')$ everywhere in the region of influence. In this case we cannot usually deblur using the previous method. That is because the phase accrual of distant points can be substantially different. We can however still deblur with high accuracy, by using local approaches. Different families of methods (28–31), have been proposed but they are all roughly equivalent in principle to deblurring using $B^H$, the the conjugate transpose of the local blurring operator. For simplicity we will refer to these methods as Conjugate Phase Reconstruction (CPR, (28)). This assumption of locally invariant convolution is akin to assuming the $B$ to be Block Circulant with Circulant blocks (BCCB). True BCCB matricies are still diagonalizable with Fourier operators and thus do not amplify noise.

Because $B$ is is assumed BCCB, $B^{-1} = F\Sigma^{-1}F^H$. In our case $\Sigma$ is the local k-space phase profile with unit magnitude. Therefore, $\Sigma^{-1} = \Sigma^*$ and $B^{-1} \approx B^H$.

Fitting linear slope to the field has been proposed (37), to further improve the previous family of methods. Incorporating corrections to the the sampling density compensation (38) often becomes necessary in these types of direct deblurring methods.

## 6.5 Separability

Another approximation that can be made when $B$ is roughly BCCB is that of separability (39). Indeed, in spiral scans, the time map $t(k) \approx Ck^2$. Since $k^2 = k_x^2 + k_y^2$, we obtain:

$$\phi(x, y, k) \approx \phi_x(x, y, k_x) + \phi_y(x, y, k_y) \tag{6.11}$$

$$psf(x, y, x', y') = FT\{e^{-i2\pi\Delta(x',y')t(k_x)}e^{-i2\pi\Delta(x',y')t(k_y)}\} \tag{6.12}$$

When $B$ is roughly BCCB, $\Delta(x', y') \approx \Delta(x, y)$ and the local psf is considered spatially invariant over the region of influence of a voxel:

$$psf(x, y) \approx FT\{e^{-i2\pi\Delta(x,y)t(k_x)}e^{-i2\pi\Delta(x,y)t(k_y)}\} = psf(x, 0) * *psf(0, y) \tag{6.13}$$

where $**$ represents a 2D convolution. This provides a significant speedup as 2D convolutions can be performed by 2 series of 1D convolutions.

## 6.6 Iterative deblurring in the presence of sharply varying off-resonance

When $\Delta(x, y)$ varies sharply, the previous methods aren't directly applicable. We will explore the iterative inversion of the system using methods of the Conjugate Gradient (CG) family. Because $B$ is not symmetric, the direct CG method is not applicable. Since $B^H B$ is always symetic, one possible solution would be to employ the CG algorithm on $B^H g = B^H B f$. This is not recommended as

$B^H B$ has $\sigma_i^2$ as singular values, which means that the condition number is also squared. This substantially slows down the convergence and increases the sensitivity to noise. The Bi-Conjugate Gradient STABilized (BICGSTAB, (40)) method is used instead to improve convergence with the non-symetric matix B.

*Implementation of the Blurring Operations*

The blurring operators $B$ and $B^H$ being large, sparse and redundant are never explicitely calculated in matrix form. A bank of kernels $k$ is precomputed for a finite set of off-resonance frequencies. The blurring operation $g = Bf$ is performed by:

$$g(i', j') = \sum_i \sum_j k_{i,j}(i - i', j - j') f(i, j) \tag{6.14}$$

and its conjugate transpose $h = B^H g$ by:

$$h(i, j) = \sum_{i'} \sum_{j'} k^*_{i,j}(i - i', j - j') g(i', j') \tag{6.15}$$

using the kernels $k$ interpolated from a finite set tabulated a priori. In regions of slowing varying off-resonance, the previous operations can be performed via 1D convolutions:

$$g(i', j') = \sum_i k_{i,j}(i - i') \sum_j k_{i,j}(j - j') f(i, j) \tag{6.16}$$

and:

$$h(i, j) = \sum_{i'} k^*_{i,j}(i - i') \sum_{j'} k^*_{i,j}(j - j') g(i', j') \tag{6.17}$$

respectively.

## 6.7 Preconditioning and Optimization

The CG algorithm can be substantially sped up by proper preconditioning. A left preconditioner is an operator $P$ that transforms the system 6.6 into:

$$P^{-1} g = P^{-1} B f \tag{6.18}$$

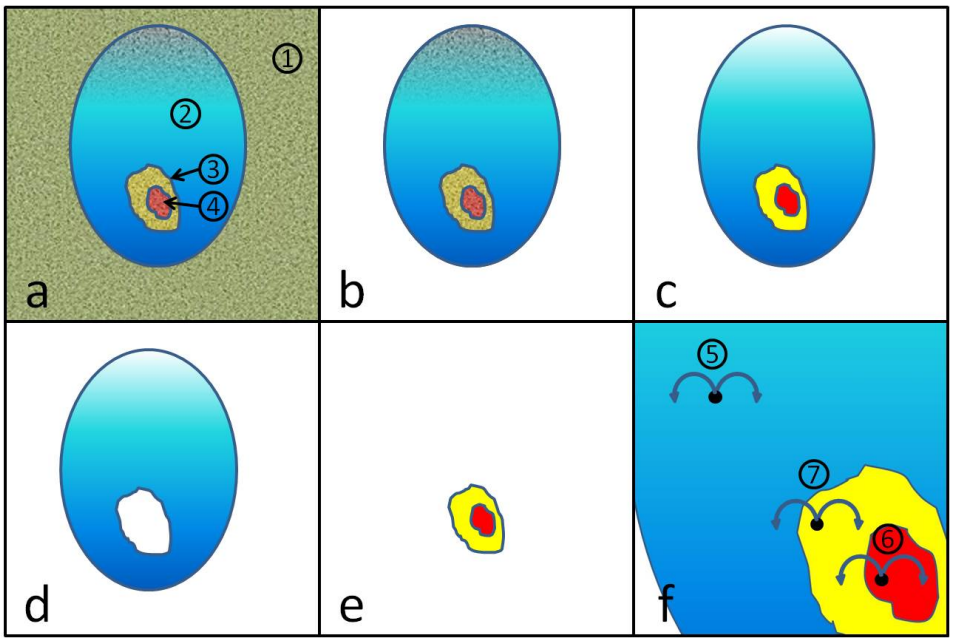


Figure 6.4: Preconditioning steps. The field map $\Delta(x, y)$ in a is first zeroed out in regions outside the head (b). The field is the denoised and its mean value is removed (c). The obtained field map is then divided in a BCCB blurring region (d) and its complement (e). The coupling of the 2 regions is illustrated in f. See text for details.

This does not change the solution to the equation but improves convergence when $P$ is chosen judiciously. Because the blurring operator B is never computed explicitly, common preconditioning methods such as those involving matrix decomposition and SVD truncations are not directly applicable. Instead, we proceed to precondition by "conditioning" the field map $\Delta$ used to generate B. Fig. 6.4 demonstrates the different preconditioning steps currently employed by our method. Fig. 6.4a represents the unfiltered field map $\Delta(x, y)$. The regions 1-4 represent air(1), an area of slowly varying field(2), an area of sharply varying field(4) and its region of influence(3). First, the regions of $\Delta$ without signal are set to 0 (6.4b). The field map is then denoised using median filtering or similar methods and is fitted to a polynomial (6.4c). The mean value of $\Delta(x, y)$ is then subtracted from it. This last step has the effect of reducing the

extent of most regions of influence. To compensate the removal of the mean off-resonance, the blurred image g is corrected using one of the previously presented spatially invariant deblurring methods (eg. 6.7) as represented by the operator $P_0^{-1}$. This is written mathematically as:

$$P_0^{-1}g = P_0^{-1}Bf \tag{6.19}$$

To simplify notations in the discussions that follow and without loss of generality, $g$ will be the corrected $P_0^{-1}g$ and $B$ will be $P_0^{-1}B$ i.e. the blurring operator obtained from the zero-mean off-resonance field $\Delta(x, y)$. Now that the regions of influence have been minimized, it is advantageous to separate the regions that can be roughly deblurred by a convolution with the conjugate transpose and the regions that can't. Define $M_\beta$ a binary mask that is 1 in the regions of sharply varying field map and their regions of influence and $M_\alpha$ its complement. Now $f$ and $\Delta$ can be split as:

$$\begin{bmatrix} f_\alpha & \Delta_\alpha \\ f_\beta & \Delta_\beta \\ f & \Delta \end{bmatrix} = \begin{bmatrix} M_\alpha \\ M_\beta \\ M_\alpha + M_\beta \end{bmatrix} [f \quad \Delta] \tag{6.20}$$

Defining $B_\alpha$ and $B_\beta$ as the blurring operators generated by $\Delta_\alpha$ (Fig. 6.4d) and $\Delta_\beta$ (Fig. 6.4e) respectively, we obtain:

$$B_\alpha + B_\beta = I + B \tag{6.21}$$

Where $I$ is the identity matrix. $g = Bf$ can thus be written[1]:

$$g = B_\alpha f_\alpha + B_\beta f_\beta \tag{6.22}$$

Because the blurring in region $\alpha$ is roughly BCCB, $B_\alpha^{-1} \approx B_\alpha^H$ and we obtain the preconditioning:

$$B_\alpha^H g = f_\alpha + B_\alpha^H B_\beta f_\beta \tag{6.23}$$

[1] Noting that $g = (B_\alpha + B_\beta - I)(x_\alpha + x_\beta)$ with $B_\alpha f_\beta = f_\beta$ and $B_\beta f_\alpha = f_\alpha$.

This constitutes a substantial speed up of the previous equation because only points in the region of sharply varying off-resonance need to be blurred at every iteration. Since $B_\alpha \approx B_\alpha^T$, the $B_\alpha^H$ operation can be further sped up by separability. The influence of the term $B_\alpha^H B_\beta f_\beta$ on region $\alpha$ is illustrated in (Fig. 6.4f). While the deblurring of point 5 would be correctly performed by CPR some areas surrounding point 7 would be incorrectly deblurred by CPR because their $B_\alpha^H$ operates on points which contain unknown contributions from region 1.

Further speedup is achieved by performing coil combination prior to deblurring. This approximation assumes slowly varying coil sensitivity in the blurring area of a voxel.

## 6.8 Fat

A challenge to deblurring is the presence of fat which blurs differently than water at a given field. One common way to deal with fat is to first perform a 3 point Dixon fat/water separation (34). The method collects images from 2 TEs at which fat and water are in and out of phase. Local field-induced phase is removed on both images which are then added and subtracted to form the fat-only and water-only images. In the presence of blur however, a fat region can blur onto a region of significantly different image phase. Therefore, phase correction cannot be performed adequately even in the presence of a perfectly known $B_0$ field map.

Our approach to deblurring in the presence of fat is to acquire images $g$ at a minimum of 2 TEs (we used 3: 3.2, 3.9 and 4.7ms) and to solve the augmented linear system:

$$\begin{bmatrix} g_{TE_1} \\ g_{TE_2} \\ g_{TE_3} \end{bmatrix} = \begin{bmatrix} BT_{Water,TE_1} & FBT_{Fat,TE_1} \\ BT_{Water,TE_2} & FBT_{Fat,TE_2} \\ BT_{Water,TE_3} & FBT_{Fat,TE_3} \end{bmatrix} \begin{bmatrix} f_{water} \\ f_{fat} \end{bmatrix} \tag{6.24}$$

Which we will write $\tilde{g} = \tilde{B}\tilde{f}$. By recognizing that:

$$\tilde{B}^H = \begin{bmatrix} T^H_{Water,TE_1}B^H & T^H_{Water,TE_2}B^H & T^H_{Water,TE_3}B^H \\ T^H_{Fat,TE_1}B^HF^H & T^H_{Fat,TE_2}B^HF^H & T^H_{Fat,TE_3}B^HF^H \end{bmatrix} \tag{6.25}$$

we can use BICGStab or similar methods to solve for $\tilde{f}$. The $F$ operator is a modulation at the off-resonance of fat (-440Hz at 3T) which requires 2 FFT operations while the $T$ operators constitute image space multiplication.

## 6.9 Water Deblurring Results

Images were acquired in a region of rapidly varying $B_0$ on GE 3T Signa Excite scanner equipped with an 8 channel head coil. Scan parameters were: TR:150ms, flip angle:$50^\circ$, FOV:24x24$cm^2$, resolution: 1x1$mm^2$. A set of 3 images was acquired at the previously mentioned TEs with a long acquisition window of 17.5ms using 80 spiral arms and a readout bandwidth of 62.5 kHz and another set was acquired with a short acquisition window of 1.64 ms using 256 spiral arms and a readout bandwidth of 250kHz. The deblurring of the blurred data took roughly 100s on an AMD Turion X2 Dual-core 2.1 GHz laptop running Matlab and the results are shown in Fig. 6.5 and in Table 6.1.

## 6.10 Discussion

The improvements resulting from by the proposed methods are most significant in regions of rapid field variation. Discrepancies between deblurring performance on synthesized and actual data are mainly due to the presence of fat, incorrect field map estimation and thru-slice dephasing.

Table 6.1: Signal/Noise Ratio (SNR), Peak SNR (PSNR) and Mean Squared Error (MRSE) of Figs. 6.5 d, a and b, respectively.

| | SNR | PSNR | MRSE |
|---|---|---|---|
| g | 9.9 | 63.7 | .0276 |
| $B^H g$ | 10.2 | 64.0 | .0257 |
| deblurred | 10.7 | 64.6 | .0227 |

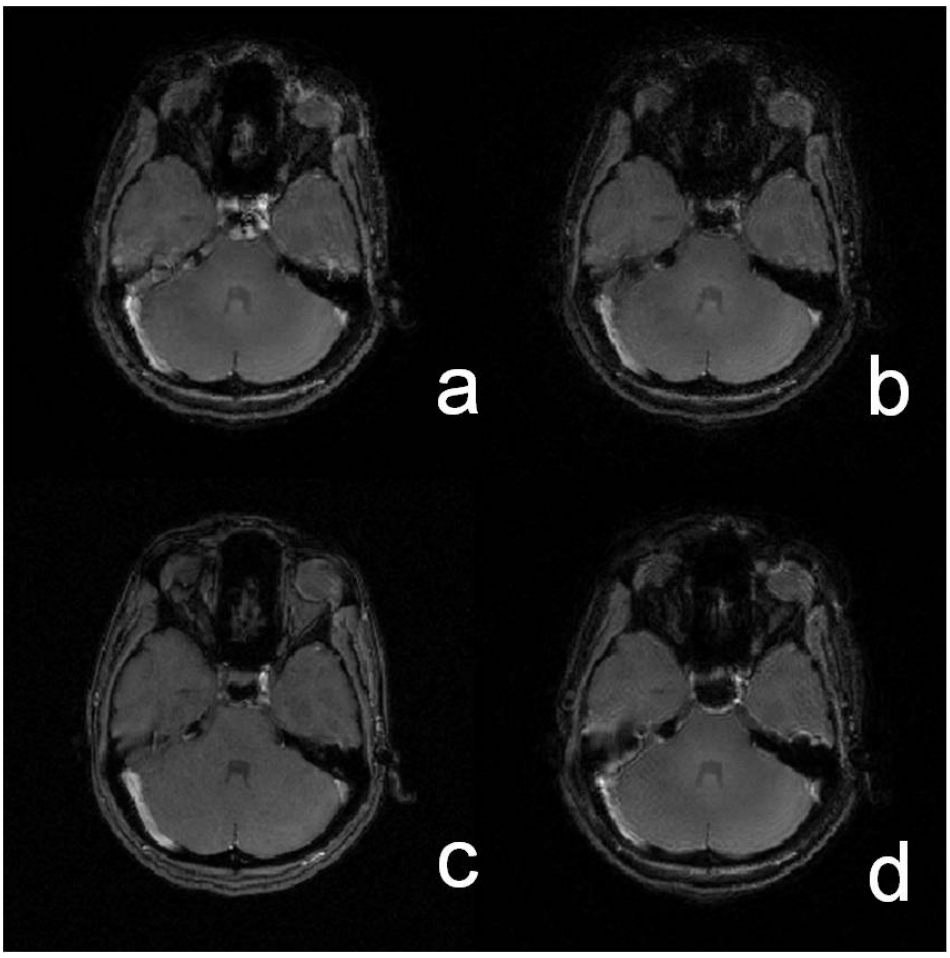


Figure 6.5: Deblurring of real images. Image deblurred using the proposed water-only method (a) and image non-iteratively deblurred by $B^H g$ (b), unblurred image (c), blurred image (d).

# Chapter 7

# CONCLUSION

SNR efficiency is a concept of high potential impact for the future of clinical MRI. Although obtaining truly SNR efficient scans of diagnostic quality remains a fundamentally unsolved problem, this work proposes methods constituting substantial steps towards this goal. A deblurring method has been proposed to allow the lengthening of non-Cartesian acquisition windows, an SNR efficient diffusion imaging method with full brain coverage and minimal distortion is explored in Chapter 4 and a simple way of increasing the speed of some 3D brain scans has been demonstrated by recognizing that some parts of k-space aren't actually useful in obtaining the reformated images and pose potential liabilities to the clinician. These techniques constitute key enabling advances towards efficient MRI sampling.

REFERENCES


[1] K. P. Pruessmann, M. Weiger, M. B. Scheidegger, and P. Boesiger, "Sense: sensitivity encoding for fast mri.," Magnetic Resonance in Medicine, vol. 42, no. 5, pp. 952–962, 1999.

[2] M. A. Griswold, P. M. Jakob, R. M. Heidemann, M. Nittka, V. Jellus, J. Wang, B. Kiefer, and A. Haase, "Generalized autocalibrating partially parallel acquisitions (grappa).," Magnetic Resonance in Medicine, vol. 47, no. 6, pp. 1202–1210, 2002.

[3] M. Lustig, D. Donoho, and J. M. Pauly, "Sparse MRI: The application of compressed sensing for rapid MR imaging.," Magn Reson Med, vol. 58, pp. 1182–1195, Dec 2007.

[4] J. Pauly, D. Nishimura, and A. Macovski, "A k-space analysis of small-tip-angle excitation," Journal of Magnetic Resonance, vol. 81, pp. 43–56, Jan. 1989.

[5] S. Conolly, D. Nishimura, and A. Macovski, "Optimal control solutions to the magnetic resonance selective excitation problem.," IEEE Transactions on Medical Imaging, vol. 5, no. 2, pp. 106–115, 1986.

[6] J. M. Pauly, P. L. Roux, D. G. Nishimura, and A. Macovski, "Parameter relations for the shinnar-le roux selective excitation pulse design algorithm," IEEE Trans Med Imaging, vol. 10, no. 1, pp. 53–65, 1991.

[7] S. Ljunggren, "A simple graphical representation of fourier-based imaging methods," Journal of Magnetic Resonance, vol. 54, no. 2, pp. 338–343, 1983.

[8] E. M. Haacke, R. W. Brown, M. R. Thompson, and R. Venkatesan, Magnetic Resonance Imaging: Physical Principles and Sequence Design. Wiley-Liss, 1999.

[9] J. I. Jackson, C. H. Meyer, D. G. Nishimura, and A. Macovski, "Selection of a convolution function for fourier inversion using gridding," IEEE Transactions on Medical Imaging, vol. 10, no. 3, pp. 473–478, 1991.

[10] J. A. Fessler, "Iterative tomographic image reconstruction using nonuniform fast fourier transforms," Biomedical Engineering, 2002.

[11] D. Rosenfeld, "An optimal and efficient new gridding algorithm using singular value decomposition.," Magnetic Resonance in Medicine, vol. 40, no. 1, pp. 14–23, 1998.

[12] D. Rosenfeld, "New approach to gridding using regularization and estimation theory.," Magnetic Resonance in Medicine, vol. 48, no. 1, pp. 193–202, 2002.

[13] J. D. O'Sullivan, "A fast sinc function gridding algorithm for fourier inversion in computer tomography.," IEEE Transactions on Medical Imaging, vol. 4, no. 4, pp. 200–207, 1985.

[14] P. J. Beatty, D. G. Nishimura, and J. M. Pauly, "Rapid gridding reconstruction with a minimal oversampling ratio.," IEEE Transactions on Medical Imaging, vol. 24, no. 6, pp. 799–808, 2005.

[15] M. A. Bernstein, K. F. King, and X. J. Zhou, Handbook of MRI Pulse Sequences, vol. 32. Elsevier Academic Press, 2004.

[16] J. A. McNab, D. Gallichan, and K. L. Miller, "3d steady-state diffusion-weighted imaging with trajectory using radially batched internal navigator echoes (turbine).," Magnetic Resonance in Medicine, vol. 63, no. 1, pp. 235–242, 2010.

[17] J. Hennig, "Multiecho imaging sequences with low refocusing flip angles," Journal of Magnetic Resonance 1969, vol. 78, no. 3, pp. 397–407, 1988.

[18] J. Hennig, Echoes - How to generate, recognize, use or avoid them in MR Imaging sequences, pp. 179–192. 1991.

[19] D. C. Alsop, "Phase insensitive preparation of single-shot rare: application to diffusion imaging in humans.," Magnetic Resonance in Medicine, vol. 38, no. 4, pp. 527–533, 1997.

[20] T. Gullion, D. B. Baker, and M. S. Conradi, "New, compensated carr-purcell sequences," J Magn Reson B, vol. 89, no. 3, pp. 479–484, 1990.

[21] A. J. Shaka, S. P. Rucker, and A. Pines, "Iterative carr-purcell trains," Journal of Magnetic Resonance 1969, vol. 77, no. 3, pp. 606–611, 1988.

[22] A. A. Maudsley, "Modified carr-purcell-meiboom-gill sequence for nmr fourier imaging applications," Journal of Magnetic Resonance 1969, vol. 69, no. 3, pp. 488–491, 1986.

[23] P. L. Roux, "Non-cpmg fast spin echo with full signal," Journal of Magnetic Resonance, vol. 155, no. 2, pp. 278 – 292, 2002.

[24] J. G. Pipe, V. G. Farthing, and K. P. Forbes, "Multishot diffusion-weighted fse using propeller mri.," Magnetic Resonance in Medicine, vol. 47, no. 1, pp. 42–52, 2002.

[25] D. A. Feinberg, B. Kiefer, and A. W. Litt, "High resolution grase mri of the brain and spine: 512 and 1024 matrix imaging.," Journal Of Computer Assisted Tomography, vol. 19, no. 1, pp. 1–7, 1995.

[26] D. K. Jones, "Diffusion mri," Diffusion MRI, vol. 2004, no. 1, pp. 37–54, 2009.

[27] J. G. Pipe and R. K. Robison, “Simplified signal equations for spoiled gradient echo mri,” ISMRM Proceedings, 2009.

[28] D. C. Noll, J. M. Pauly, C. H. Meyer, D. G. Nishimura, and A. Macovskj, “Deblurring for non-2D fourier transform magnetic resonance imaging,” Magnetic Resonance in Medicine, vol. 25, no. 2, pp. 319–333, 1992.

[29] Y. M. Kadah and X. Hu, “Simulated phase evolution rewinding (sphere): A technique for reducing b0 inhomogeneity effects in mr images,” Magnetic Resonance in Medicine, vol. 38, no. 4, pp. 615–627, 1997.

[30] L.-C. Man, J. M. Pauly, and A. Macovski, “Multifrequency interpolation for fast off-resonance correction,” Magnetic Resonance in Medicine, vol. 37, no. 5, pp. 785–792, 1997.

[31] H. Moriguchi, B. M. Dale, J. S. Lewin, and J. L. Duerk, “Block regional off-resonance correction (brorc): A fast and effective deblurring method for spiral imaging,” Magnetic Resonance in Medicine, vol. 50, no. 3, pp. 643–648, 2003.

[32] M. K. Makhijani and K. S. Nayak, “Exact correction of sharply varying off-resonance effects in spiral mri,” in Proc. 3rd IEEE Int Biomedical Imaging: Nano to Macro Symp, pp. 730–733, 2006.

[33] J. A. Fessler, S. Lee, V. T. Olafsson, H. R. Shi, and D. C. Noll, “Toeplitz-based iterative image reconstruction for mri with correction for magnetic field inhomogeneity,” vol. 53, no. 9, pp. 3393–3402, 2005.

[34] T. W. Dixon, “Simple proton spectroscopic Imaging,” Radiology, vol. 153, pp. 189–194, 1984.

[35] Y. M. Kadah and X. Hu, “Algebraic Reconstruction for Magnetic Resonance Imaging under B0 Inhomogeneity,” IEEE Trans. Med. Imaging, vol. 17, no. 3, pp. 362–370, 1998.

[36] J. G. Nagy and D. P. O’Leary, “Restoring Images Degraded by Spatially Variant Blur,” SIAM J. Sci. Comput., vol. 19, pp. 1063–1082, July 1998.

[37] P. Irarrazabal, C. H. Meyer, D. G. Nishimura, and A. Macovski, “Inhomogeneity correction using an estimated linear field map.,” Magnetic Resonance in Medicine, vol. 35, no. 2, pp. 278–282, 1996.

[38] D. C. Noll, J. A. Fessler, and B. P. Sutton, “Conjugate phase mri reconstruction with spatially variant sample density correction.,” IEEE Transactions on Medical Imaging, vol. 24, no. 3, pp. 325–336, 2005.

[39] E. Ahunbay and J. G. Pipe, “Rapid method for deblurring spiral MR images,” Magnetic Resonance in Medicine, vol. 44, no. 3, pp. 491–494, 2000.

[40] H. A. V. D. Vorst, “Bi-cgstab: A fast and smoothly converging variant of bi-cg for the solution of nonsymmetric linear systems,” SIAM J Sci Stat Comput, vol. 13, no. 2, pp. 631–644, 1992.

## BIOGRAPHICAL SKETCH

Eric Aboussouan grew up near Montreal, Canada. He studied Computer Engineering at the Ecole Polytechnique de Montréal, Canada and the Luleå Tekniska Universitet, Sweden. He also holds a Master's degree in Biomedical Engineering from the NanoRobotics Lab at the Ecole Polytechnique de Montréal where he conducted research on untethered vascular microdevices for targeted drug delivery. He then moved to Phoenix, Arizona to join the Barrow Neurological Institute where his work involved spiral imaging deblurring and 3D diffusion weighted imaging in the brain.